SIAM J. Applied Dynamical Systems
Vol. 4, No. 4, pp. 1195–1228

Kink-Antikink Collisions in the ϕ^4 Equation: The n-Bounce Resonance and the Separatrix Map*

Roy H. Goodman† and Richard Haberman‡

Abstract. We provide a detailed mathematical explanation of a phenomenon known as the two-bounce resonance observed in collisions between kink and antikink traveling waves of the ϕ^4 equations of mathematical physics. This behavior was discovered numerically in the 1980s by Campbell and his collaborators and subsequently discovered in several other equations supporting traveling waves. We first demonstrate the effect with new high-resolution numerical simulations. A pair of kink-like traveling waves may coalesce into a localized bound state or may reflect off each other. In the two-bounce resonance, they first coalesce, but later escape each other's embrace, with a very regular pattern governing the behaviors. Studying a finite-dimensional "collective coordinates" model, we use geometric phase-plane based reasoning and matched asymptotics to explain the mechanism underlying the phenomenon, including the origin of several mathematical assumptions needed by previous researchers. We derive a separatrix map for this problem—a simple algebraic recursion formula that explains the complex fractal-like dependence on initial velocity for kink-antikink interactions.

Key words. solitary waves, nonlinear resonance, separatrix map, singular perturbation theory

AMS subject classifications. 74J35, 70K44, 37D45

DOI. 10.1137/050632981

1. Introduction.

In this paper, we provide a complete description of the mechanism underlying a phenomenon known as the two-bounce resonance in the ϕ^4 equations, a strongly nonlinear dispersive wave equation with a double-well potential:

$$\phi_{tt} - \phi_{xx} - \phi + \phi^3 = 0. \tag{1}$$

This phenomenon was first described by Campbell and his many collaborators in a remarkable series of papers in the 1980s [9, 10, 11, 38] and further elaborated by Anninos, Oliveira, and Matzner [4]. We begin with a demonstration of the phenomenon, before describing its history and putting the equation in context.

Equation (1) supports a family of traveling wave solutions (kinks)

$$\phi(x,t) = \phi_K(x - vt) = \tanh\left(\xi/\sqrt{2}\right), \tag{2}$$

where $\xi = (x - x_0 - vt)/\sqrt{1-v^2}$ for any fixed velocity v, $-1 < v < 1$. The antikink solution is a traveling wave of the opposite orientation, $\phi_{\bar{K}} = -\phi_K$. Each of these asymptotes to ± 1, the only fixed points of (1), and we may ask what happens when a kink and an antikink

*Received by the editors June 2, 2005; accepted for publication (in revised form) by T. Kaper August 1, 2005; published electronically November 22, 2005.
http://www.siam.org/journals/siads.4-4/63298.html
†Department of Mathematical Sciences, New Jersey Institute of Technology, Newark, NJ 07102 (goodman@njit.edu). The work of this author was supported by NSF-DMS 0204881.
‡Department of Mathematics, Southern Methodist University, Dallas, TX 75275 (rhaberma@mail.smu.edu).

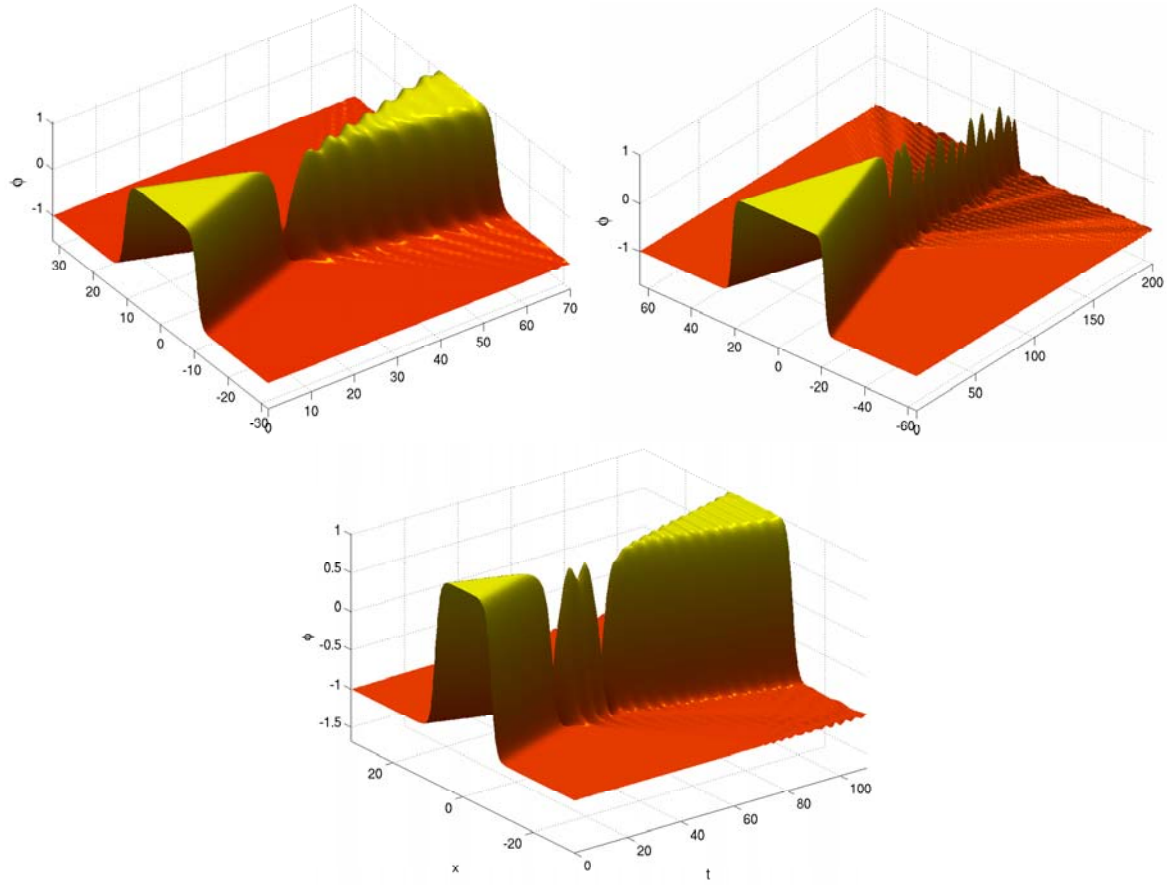

Figure 1. *A collision between a kink and an antikink with* (a) $v = 0.35$*, showing reflection with one collision (or bounce),* (b) $v = 0.213$*, leading to the mutual capture of the pair, with a large amount of radiation shed, and* (c) $v = .1988$*, the two-bounce resonance.*

collide. In the closely related sine-Gordon equation, collisions are well understood because the equation's complete integrability severely constrains the dynamics [15]; their behavior will be described below. To explain the more diverse behavior in ϕ^4 collisions, we begin with some numerical simulations, details of which are described in Appendix A. A kink and an antikink are initialized propagating toward each other with speed v:

$$\phi(x,0) = \phi_K(x + x_0) + \phi_{\bar{K}}(x - x_0) - 1 \tag{3}$$

with an equivalent initial condition for $\phi_t(x, 0)$.

At large speeds, the two waves are immediately reflected upon collision, as seen in part (a) of Figure 1. Below some critical speed v_c, the two waves may form into a sort of chaotic bound state, as seen in part (b) of the figure. What is most interesting is that for certain initial velocities, which fall into a discrete set of so-called resonance windows, the kink and antikink collide, begin to move apart, but then turn around and collide a second time before finally escaping from each other's influence, as seen in part (c) of Figure 1. Because the two

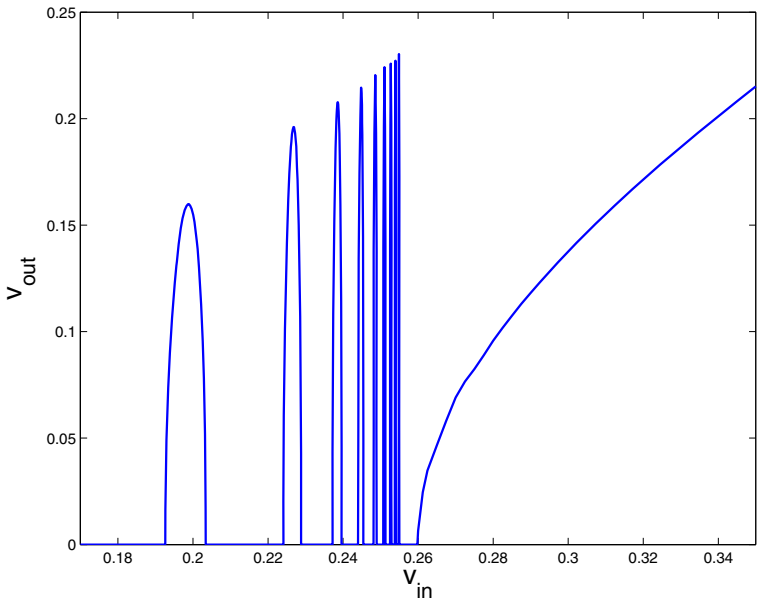

Figure 2. *The output velocity as a function of the input velocity, showing a critical velocity of about* $v_c = .2598$ *and several two-bounce resonance windows. (Some details have been suppressed for clarity of exposition. This will be discussed later.)*

waves seem to bounce off each other twice, this phenomenon is known as the two-bounce resonance.

A summary of this behavior is shown in Figure 2 in which the outgoing speed of the kink and antikink (postinteraction) is plotted as a function of the incoming speed. The critical velocity is seen to be $v_c = 0.2598$. The intervals of initial velocities for which the kinks escape each other's influence after two interactions were termed *two-bounce windows* by Campbell et al. or, more generally, resonance windows. The resonance windows furthest from the critical velocity are the widest, and they decrease in width with increasing velocity. Figure 1(c) shows a simulation with initial velocity residing in the first two-bounce window. The bound state that is formed after the first collision undergoes two internal oscillations before being extinguished on the second bounce. Figure 3 depicts a resonant solution from the second window. The bound state clearly undergoes three internal oscillations. Evidently, during the first collision, the kink and antikink lose kinetic energy to a secondary mode of oscillation, and if the timing is right, they regain that energy on the second bounce. Figure 2 shows the first ten resonance windows; in each subsequent window, the bound state undergoes one additional oscillation before the two kinks collide a second time and separate.

In fact the behavior is significantly more complicated than just described. In addition to the two-bounce windows, there exist families of three-bounce windows, which feature three exchanges of energy. The three-bounce windows are situated around the edges of the two-bounce windows, and seem to accumulate at the edges of the two-bounce windows, much as the two-bounce windows accumulate just below the critical velocity. Two examples of three-bounce solutions are shown in Figure 4, as well as the three-bounce window structure

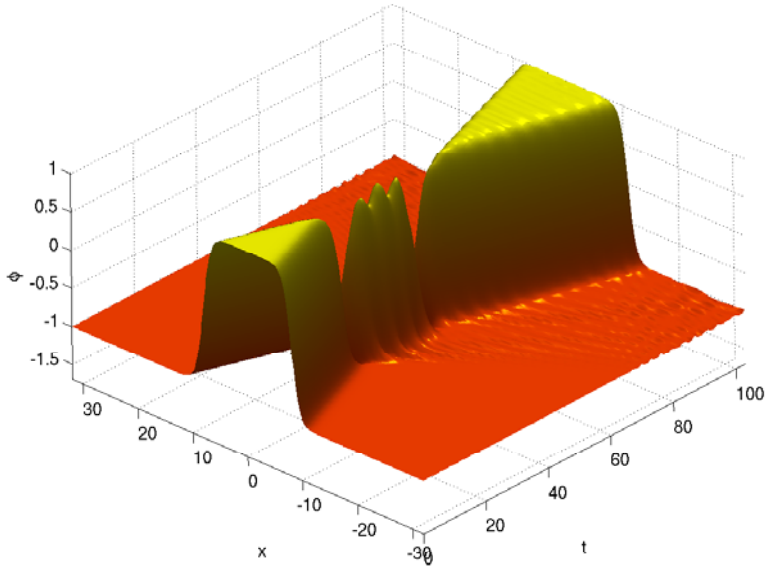

Figure 3. *A collision with $v = .2269$, showing clearly that the bound state undergoes three oscillations in the interval between the two collisions. Compare with Figure 1(c), in which the bound state undergoes two oscillations.*

surrounding the first two-bounce window, a structure which has been omitted from Figure 2. We will show later that, while there is only one type of two-bounce window, the spectrum of three-bounce window types is much wider.

The purpose of the paper is to present an explanation of the phenomenon demonstrated above based on dynamical systems perturbation theory and matched asymptotic expansions, using and extending ideas we have applied previously in [21, 22]. It is organized as follows. In section 2, we review the ϕ^4 equation, the two-bounce resonance phenomenon, and the findings of previous researchers. In section 3 we describe a "collective coordinates" model, a system of ordinary differential equations (ODEs) shown by Anninos, Oliveira, and Matzner to capture all the relevant dynamics [4]. In section 4, we generalize the ODE model by introducing a free parameter, and we use a Melnikov energy integral to derive a formula for the critical velocity. The dependence on this additional parameter yields significant insight into the mechanism underlying capture. This approach is extended in section 5 in which matched asymptotics are used to construct two-bounce resonant solutions, which yields a formula for the resonant velocity windows. This is then extended to general, nonresonant initial conditions in section 6, where we derive the separatrix map for this problem, an algebraic recursion formula that reproduces much of the structure of the ODE simulations. We make some concluding remarks in section 7. Appendix A describes some details of the methods used in the simulation of ODEs and partial differential equations (PDEs) discussed here.

2. Scientific background. The ϕ^4 equation arises in many contexts and is often used as a phenomenological model, as it is the simplest nonlinear dispersive PDE that supports kink-shaped traveling waves. Kink waves are topological entities, defined by their boundary conditions at infinity and describable in terms of a winding number, and are thus useful as a

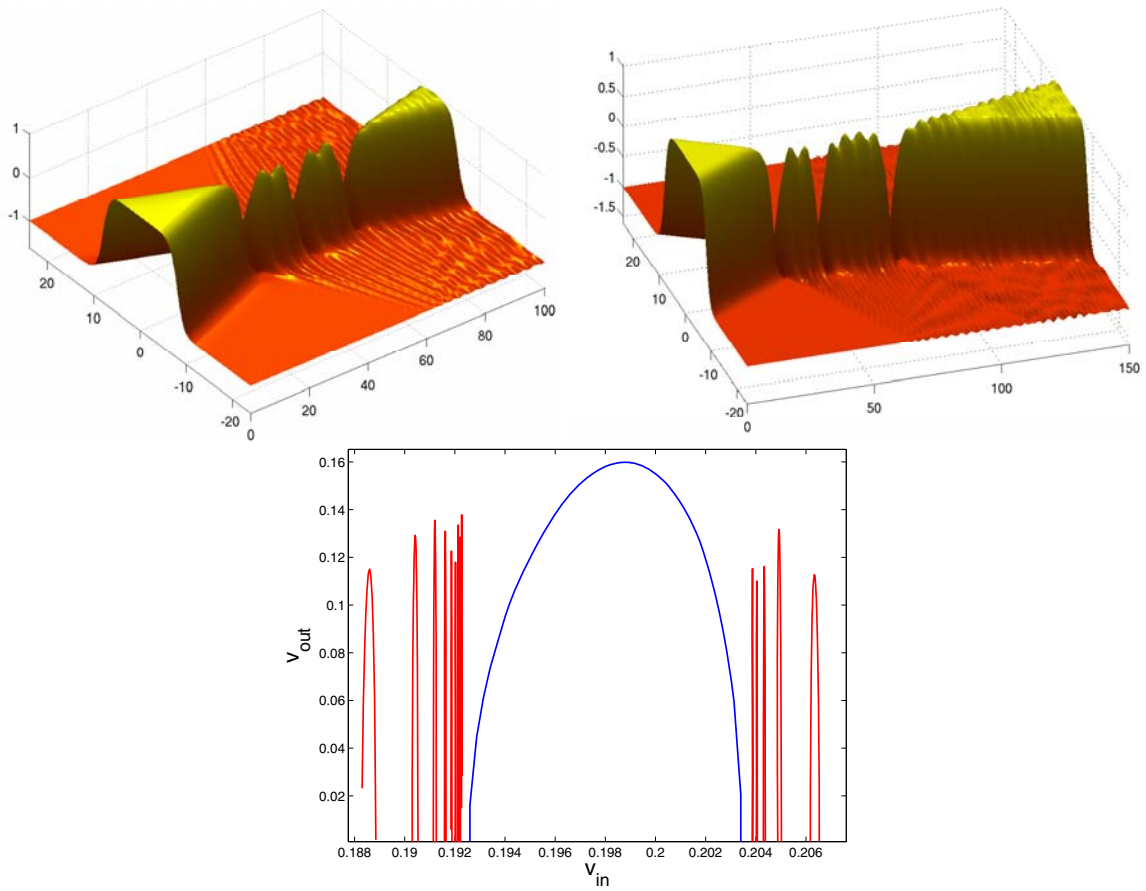

Figure 4. *Two examples of three-bounce solutions, with initial velocities* $v = 0.1886$ *and* $v = 0.19125$*, and the three-bounce windows surrounding the first two-bounce window in Figure 2.*

simple model in theoretical nuclear physics. In cosmology, it is used to model domain walls, simple structures that may be important in the evolution of structure in the universe [4]. A summary of around ten applications is described in the introduction to [11].

Once a dispersive nonlinear wave equation has been shown to support localized traveling wave solutions, a question that naturally follows is how two such waves interact upon collision. The notes of John Scott Russell, who first observed solitary waves in shallow water in 1834 [42], contain sketches of a fast solitary wave passing through a slower one. The modern study of solitary wave interactions begins with the pioneering numerical experiments by Zabusky and Kruskal of the Korteweg–de Vries equation, which models, among other things, Russell's experiments [51] and oscillations in Fermi–Pasta–Ulam lattices. They found, as was later shown to be typical of completely integrable systems, that two solitary waves pass through each other upon collision, unscathed but for a finite shift in their positions relative to their trajectories. They called these waves solitons, and exact solutions describing the collision of two solitons were found soon after by Gardner, Greene, Kruskal, and Miura [20], who

first developed the inverse scattering transform technique. Exact kink-antikink and two-kink solutions of the sine-Gordon equation show that kinks repel each other, while kinks and antikinks attract each other [15, 29, 37]. Collisions in completely integrable systems are remarkable for the near-total lack of radiation shed following a collision. Solitons have a fascinating history that is well accounted in [2, 35, 43] and elsewhere.

Unlike the closely related sine-Gordon equation, the ϕ^4 equation is not completely integrable. Collisions in nonintegrable systems can lead to a far richer set of behaviors. Colliding waves may, as we have seen, be captured forever, or for a finite time in the case of two-bounce solutions. Solitons may pass through each other, or be reflected, similarly to solitons. In addition, they may simply be destroyed, as, it could be argued, happens in Figure 1(c). Completely integrable systems have extremely nongeneric behavior. They are severely constrained by an infinite sequence of independent conservation laws. Solitary waves in nonintegrable systems often possess internal modes, which manifest themselves as oscillations in the shape, amplitude, or speed of the waves. Such modes are absent in integrable systems, but coupling to the continuous spectrum can play much the same role in nonintegrable systems that lack discrete oscillation modes [45, 50, 47]. The production of radiation is generally much stronger in nonintegrable systems, and the internal modes often play an important role in transferring energy from solitary waves to the continuum.

Solitary wave collisions, and the closely related problem of solitary wave interactions with localized imhomogeneities, continue to attract a large amount of attention; see [29] and references therein. In addition to the examples already cited, they have been investigated in a wide variety of settings, including Fermi–Pasta–Ulam lattices [14, 19] and Bragg grating optical fibers [24]. Curved waveguides in long Josephson junctions have been shown to induce a potential that may be used to trap solitons whose evolution is described by the sine-Gordon equation [25]. In recent years, Bose–Einstein condensates have provided a tantalizing new application for theoretical and experimental studies of nonlinear waves, including their trapping and interaction [1, 6]. Another way of adding a small amount of nonintegrability into a system is by replacing spatial derivatives with discrete difference formulas, yielding a large coupled system of ODEs. Interesting interactions between solitary waves in such systems have been found in [7] and [36].

2.1. The two-bounce resonance. The two-bounce resonance phenomenon was discovered by a group from Los Alamos and examined in a large group of papers, each with a slightly different set of authors, though Campbell and/or Peyrard appear in each [9, 10, 38, 39]. The existence of the phenomenon was hinted at by earlier numerical experiments by Ablowitz, Kruskal, and Ladik several years earlier, but was confined to a single remark, due to limitations at that time in computation and visualization [3]. The most relevant study in the present case is the first paper in the series [11] by Campbell, Schonfeld, and Wingate. They showed that collisions between kinks and antikinks may display the two-bounce resonance behavior in several different nonlinear Klein–Gordon equations—wave equations in which the ϕ-dependent potential energy has two or more local minima of equal depth connected by a heteroclinic orbit. For example, the ϕ^4 equation conserves an energy E with a dual-well potential $V(\phi)$,

$$E = \frac{\phi_x^2}{2} + \frac{\phi_t^2}{2} + V(\phi) = \frac{\phi_x^2}{2} + \frac{\phi_t^2}{2} - \frac{\phi^2}{2} + \frac{\phi^4}{4},$$

and the kink and antikink are heteroclinic orbits connecting the minima of V at $\phi = \pm 1$.

They showed, through a series of numerical experiments on kink-antikink interactions in nonlinear Klein–Gordon equations with different potentials $V(\phi)$, that a necessary condition for the two-bounce resonance to exist is for the kink to support an oscillatory internal mode, into which kinetic energy can be transferred during the collision. This in effect robs the kink and antikink of the energy they need to overcome their mutual attraction. They showed that the interaction leads to a resonant reflection if the time between the first and second collision satisfies a relation of the form

$$\frac{t_2 - t_1}{\omega} = 2\pi n + \delta, \tag{4}$$

where the parameters ω and δ are found by a least-squares fit. They found that $2\pi\omega \approx 5.23$, very close to $2\pi\omega = 2\pi\sqrt{2/3} \approx 5.13$, the value that would arise due to the internal mode frequency derived below. Thus, this condition states that the internal mode must oscillate an integer number of times plus some constant offset δ. They derived a remarkably accurate formula for the resonant velocities using (4) and the numerically obtained value of the critical velocity, which was used in our computations for Figure 2. Their predicted values for v_n lay inside the resonance window for all values of n we examined—up to $n = 15$! Essentially, once the first few window locations are known, the least-squares fit is used to find ω and δ, which can then be used to predict the subsequent windows. Among the other strengths of our analysis, it provides formulas for both v_c and δ without requiring any constants to be found by least-squares fitting. A subsequent study by Anninos, Oliveira, and Matzner found that there exist many additional, much narrower *three*-bounce windows in between the two-bounce windows [4], and that between these are four-bounce windows and so on, all of which combine to form an intricate fractal structure of reflection windows. They further showed, by numerical calculation of Lyapunov exponents, that a trapped solution of the type pictured in Figure 1(b) can be considered chaotic. They used a more accurate numerical scheme and further analyzed the problem using an ODE model. We will focus on this ODE model to explain the origin of the window structure and derive a very simple recursion relation that describes all of this structure's major features.

Two-bounce resonant behavior was subsequently discovered numerically in the collisions of sine-Gordon kinks with localized defects in work by Fei, Kivshar, and Vázquez [17, 18, 30] and later in collisions of orthogonally polarized vector solitons in birefringent optical fibers by Tan and Yang [50, 45]. We have considered these problems in recent publications [21, 22]. Each of those systems features a small parameter ϵ which measures the strength of the coupling between translation and oscillation modes, as well as the disparity between the associated timescales. This parameter allowed us to derive analytically very precise asymptotic statements about the behavior of collisions in the limits of small ϵ. The ϕ^4 model contains no small parameter. We will add one artificially to the model ODE described in the next section and show that the small ϵ perturbation theory, similar to that used in [21, 22], works qualitatively up to $\epsilon = O(1)$, so that the conclusions are still valid when the small parameter is removed.

2.2. Internal modes. The Campbell studies show that the two-bounce phenomenon arises due to a temporary transfer of energy to a secondary mode of oscillation—a reservoir from

which the energy is extracted on the second bounce. If a kink solution is perturbed by a small amount $\phi(x,t) = \phi_K(\xi) + \chi(\xi)e^{-i\omega t}$, then χ approximately satisfies (1) linearized about $\phi_K(\xi)$. This takes the form of a Schrödinger eigenvalue problem with a reflectionless potential:

$$(\omega^2 - 2)\chi = \left(-\partial_x^2 + -3\,\mathrm{sech}^2\,(\xi/\sqrt{2})\right)\chi. \tag{5}$$

This has two discrete eigenmodes. The first, with $\omega_0 = 0$, arises from the translation invariance of (1) and does not participate in the dynamics. The second has eigenvalue $\omega_1 = \sqrt{\frac{3}{2}}$ and eigenfunction

$$\chi_1(\xi) = \left(\frac{3}{\sqrt{2}}\right)^{1/2} \tanh\xi\,\mathrm{sech}\,\xi. \tag{6}$$

3. The Anninos–Oliveira–Matzner ODE model. Anninos, Oliveira, and Matzner performed direct numerical experiments of the two-bounce phenomenon and found additional three-bounce resonances and a fractal structure we will discuss and explain in sections 6.2 and 6.3. Most of their analysis concerns a collective coordinate model with two degrees of freedom derived using the so-called variational approximation, as will ours.[1] This method may be used in PDE systems that minimize a Lagrangian action, in the case that the dynamics are known empirically to exhibit an underlying low-dimensional behavior. An extensive exposition of this method is given in a recent review article by Malomed [32].

The variational approximation method assumes that the solution can be well approximated by a functional form that depends on a few time-dependent parameters. This ansatz is then substituted into the Lagrangian density and integrated with respect to the space variables in order to obtain an effective finite-dimensional Lagrangian whose Euler–Lagrange equations describe the evolution of the parameters. Essentially, this minimizes the Lagrangian action within a severely constrained class of functions. If the initial conditions are well represented by the ansatz, and the PDE's solution stays close to the ansatz for the time considered, this may be expected to provide useful insights. The resulting ODEs should be thought of as a model of the PDE behavior, rather than as a faithful approximation. No theorems exist to guarantee that a solution to the finite-dimensional system approximates the behavior of the full system, but it often works well in practice.

The ϕ^4 equation (1) minimizes the action due to the Lagrangian density

$$\mathcal{L} = \frac{1}{2}\phi_t^2 - \frac{1}{2}\phi_x^2 + \frac{1}{2}\phi^2 - \frac{1}{4}\phi^4. \tag{7}$$

Following [4, 5, 44], we take an ansatz consisting of a kink and an antikink at an undetermined position $X(t)$ as well as two internal modes of undetermined amplitude $A(t)$, each moving in unison with its associated kink:

$$\phi_{\text{ansatz}}(x,t) = \phi_K(x + X(t)) - \phi_K(x - X(t)) + 1 + A(t)\big(\chi_1(x + X(t)) - \chi_1(x - X(t))\big). \tag{8}$$

[1] This model was also studied by Sugiyama [44] and Belova and Kudryatsev [5], prior to the work of Anninos, Oliveira, and Matzner, but the paper of Anninos, Oliveira, and Matzner is the closest antecedent to our present approach. A related collective coordinate model appears in Campbell, Schonfeld, and Wingate [11].

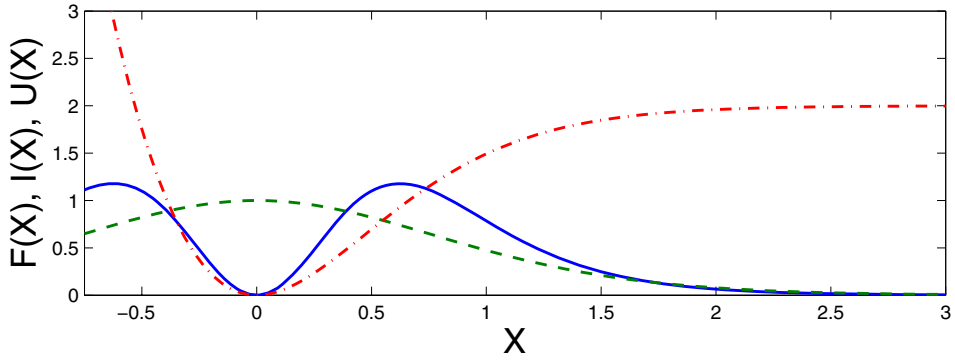

Figure 5. *The potential and coupling functions, $F(x)$ (blue, solid), $I(x)$ (green, dashed), and $U(x)$ (red,dash-dot).*

Substituting this expression into the Lagrangian (7) and integrating x from $-\infty$ to ∞ yield the effective Lagrangian

$$L_{\text{eff}}(X,\dot{X},A,\dot{A}) = M(1+I(X))\dot{X}^2 - MU(X) + \dot{A}^2 - \omega^2 A^2 + 2M^{-1/2}F(X)A, \tag{9}$$

where

$$\begin{aligned} I(X) &= 3\,\mathrm{sech}^2\,\alpha(\alpha - \tanh\alpha)\coth^3\alpha, \\ U(X) &= 6\left[-\frac{2}{3} + \alpha + 3\coth\alpha - (2+3\alpha)\coth^2\alpha + 2\alpha\coth^3\alpha\right], \\ F(X) &= \frac{3\pi}{2}\tanh^2\alpha\,\mathrm{sech}^2\,\alpha, \end{aligned} \tag{10}$$

$\alpha = \sqrt{2}X$, and the constants are defined by

$$M = \frac{2\sqrt{2}}{3} \text{ and } \omega = \sqrt{\frac{3}{2}} \tag{11}$$

corresponding to the eigenvalue in (6). We have departed slightly from the notation of previous authors by making the three functions $I(X)$, $U(X)$, and $F(X)$ independent of M and putting the M-dependence directly into the Lagrangian (9). These functions are shown in Figure 5. We generalize the equations slightly by allowing ω to depend on a parameter ϵ,

$$\omega = \sqrt{\frac{3}{2}}\Big/\epsilon. \tag{12}$$

We will see that when $0 < \epsilon \ll 1$, this leads to a wide disparity between the timescales of the two modes, leading to weak coupling, so we will be able to use perturbation methods, which work well even when $\epsilon = O(1)$.

The Euler–Lagrange equations for the Lagrangian (9) describe the evolution for X and A:

$$\ddot{X} = \frac{1}{D(X)}(-I'(X)\dot{X}^2 - U'(X) + 2M^{-3/2}F(X)'A), \tag{13a}$$

$$\ddot{A} + \omega^2 A = F(X), \tag{13b}$$

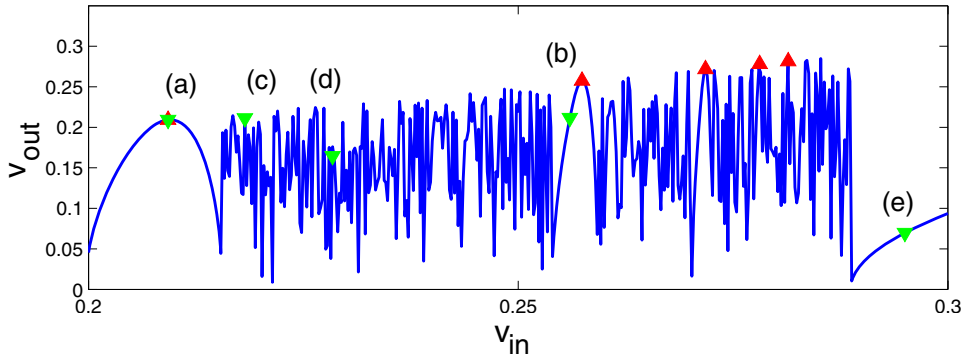

Figure 6. *The input velocity versus the output velocity for the ODE model (13) with $\epsilon = 1$ and initial condition (14). The first few window centers are indicated in red. The points marked in green correspond to the plots in Figure 7.*

where $D(X) = 2(1 + I(X))$. This system conserves a Hamiltonian (not written here in canonical form),

$$H(X, \dot{X}, A, \dot{A}) = \frac{MD(X)}{2}\dot{X}^2 + MU(X) + \dot{A}^2 + \omega^2 A^2 - \frac{2}{\sqrt{M}}F(X)A.$$

We note that $I(X)$ and $F(X)$ decay to zero exponentially as $|X| \to \infty$, while $U(X) \to 2$ as $X \to \infty$ and $U(X)$ grows linearly as $X \to -\infty$. Therefore X is bounded from below for any solution with finite energy—the kinks can penetrate past each other only a finite distance. The energy is not positive definite, but it is in the limit as $X \to +\infty$, so that when the kinks are far apart, the energy can be partitioned into positive X and A components.

We simulate the dynamics of (13), along with the "initial conditions" as $t \to -\infty$,

$$X \sim X_0 - Vt;\ \dot{X} \to -V;\ A \to 0;\ \dot{A} \to 0. \tag{14}$$

In practice, we start at $t = 0$ with $X = 10$, $\dot{X} = -V$, and $A = \dot{A} = 0$, although the results are not sensitive to the initial value of X if it is chosen sufficiently large. The analogue of Figure 2 for numerical simulations of the ODE model is shown in Figure 6 for the case $\epsilon = 1$. The behavior of this model mimics that of the PDE simulations. Above a critical velocity $v_c \approx 0.289$, the two kinks reflect off each other with just one bounce, while below that they capture each other and interact for a longer period. While the behavior in the regions between the windows is clearly more complex than that of the PDE simulations, the two-bounce resonance windows persist, as do some of the narrower windows. There exists a sequence of two-bounce windows of decreasing width at velocities closer and closer to the critical value, the first five of which are marked in the figure.

In Figure 7, we show several numerical solutions to the ODE (13) with initial conditions (14), corresponding to the marked points in Figure 6. In column (a) the first two-bounce resonant solution is plotted. The speed at which the solitons eventually escape is exactly equal to their input speed and $A(t)$ returns to its rest state as $t \to \infty$. After the complicated transition, $A(t)$ undergoes about one full oscillation. The two "bounce times" at which X achieves

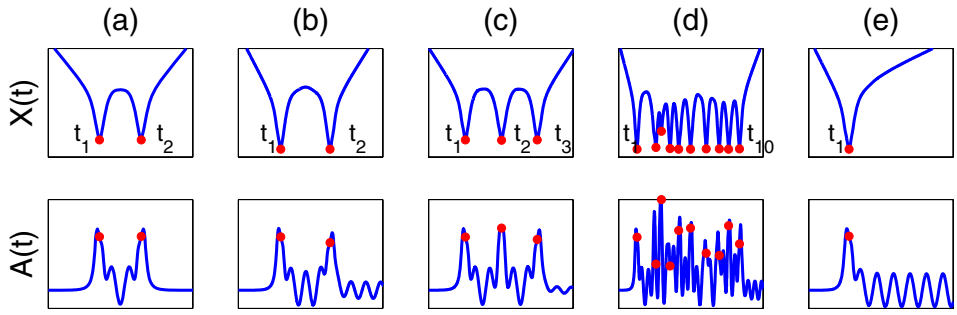

Figure 7. *Five solutions to (13), corresponding to the five marked initial values in Figure 6. Explanations are given in the text.*

its local minima are marked as t_1 and t_2. The other images are marked similarly. Column (b) is from within the second resonance window, but not quite on the resonance, and illustrates two facts. First, $A(t)$ undergoes one more complete oscillation than the solution in the first window, and second, since this initial condition is not quite resonant, $A(t)$ does not return to zero as $t \to +\infty$. In column (c), we have plotted a nearly resonant three-bounce solution. Column (d) shows a solution with ten bounces, and column (e) shows a solution with the initial speed greater than v_c, in which the solitons bounce off each other just once.

We note that the point $(+\infty, 0, 0, 0)$ is a degenerate saddle-center in the four-dimensional dynamics. The two- and three-bounce resonant solutions discussed above are homoclinic orbits to the invariant manifold $(+\infty, \dot{X}, 0, 0)$. Homoclinic orbits to (nondegenerate) saddle-centers have been previously studied by many (see, for example, [48]). Embedded solitons may also be thought of as homoclinic orbits to saddle-centers [49].

A reconstruction of the wave field from a solution to the ODE (13) with two-bounce resonant initial velocity (corresponding to point (a) in Figure 6) is shown in Figure 8. In fact, the entire structure is composed of many windows of varying widths. True capture is possible for the ODE system only on a set of initial conditions with measure zero, by reasoning similar to the Poincaré recurrence theorem of Hamiltonian mechanics [23].

Before proceeding, we first make note of a few scalings of the evolution equation (13) that will be important in different parts of the phase space. First, we introduce polar coordinates J and θ in the A-$\dot{A}$ variables $A = J\cos\theta$ and $\dot{A} = \omega J \sin\theta$, under which (13) becomes

$$\begin{aligned} D(X)\ddot{X} &= -I'(X)\dot{X}^2 - U'(X) + 2M^{-3/2}F(X)J\cos\theta; \\ \dot{J} &= \frac{1}{\omega}F(X)\sin\theta; \\ \dot{\theta} &= -\omega + \frac{\cos\theta}{\omega J}. \end{aligned} \tag{15}$$

As always with polar coordinates, these equations become degenerate near $J = 0$. If we make

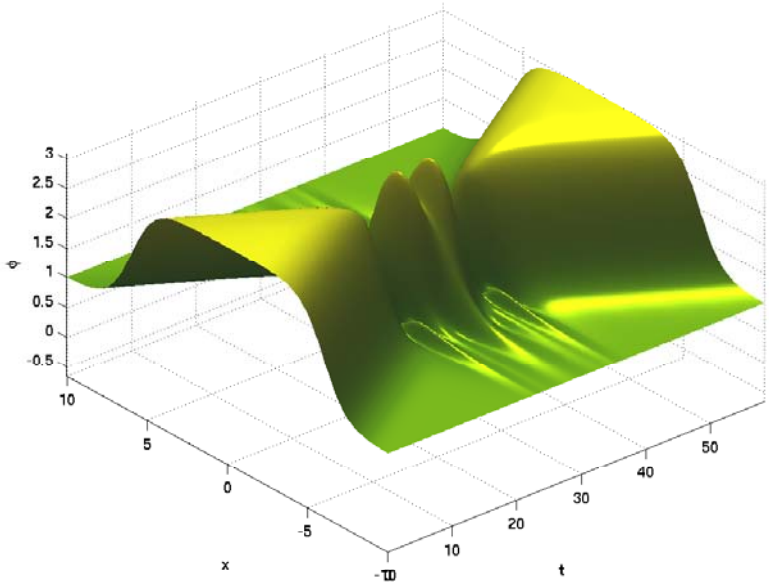

Figure 8. *The full solution reconstructed from the finite-dimensional model (13), with initial velocity $v = 0.2093$, at the center of the first resonance window in Figure 6.*

the scaling $J_{\text{in}} = \omega J$, then (15) becomes

$$
\begin{aligned}
D(X)\ddot{X} &= -I'(X)\dot{X}^2 - U'(X) + \frac{2}{\omega}M^{-3/2}F(X)J_{\text{in}}\cos\theta;\\
\dot{J}_{\text{in}} &= F(X)\sin\theta;\\
\dot{\theta} &= -\omega + \frac{\cos\theta}{J_{\text{in}}},
\end{aligned}
\tag{16}
$$

which is the scaling implicitly assumed in the remainder of this section, and will form the "inner approximation" in our matched asymptotic expansion. Note that in the limit as $\omega \to \infty$, X evolves independently of J_{in} and θ, but J_{in} and θ depend on X. Finally, the scaling $J_{\text{out}} = \sqrt{\omega}J$ leads to

$$
\begin{aligned}
D(X)\ddot{X} &= -I'(X)\dot{X}^2 - U'(X) + \frac{2}{\sqrt{\omega}}M^{-3/2}F(X)J_{\text{out}}\cos\theta;\\
\dot{J}_{\text{out}} &= \frac{1}{\sqrt{\omega}}F(X)\sin\theta;\\
\dot{\theta} &= -\omega + \frac{\cos\theta}{\sqrt{\omega}J_{\text{out}}}.
\end{aligned}
\tag{17}
$$

This will form the "outer approximation" in our matched asymptotic expansion. In the limit as $\omega \to \infty$, X evolves independently of J_{in} and θ, and vice-versa.

4. Calculation of the energy change and critical velocity. The Lagrangian (9) contains two degrees of freedom X and A coupled only through the final term $2M^{-1/2}F(X)A$. If the frequency is very large, $\omega \gg 1$, the coupling between the two modes is weak, since (21), which

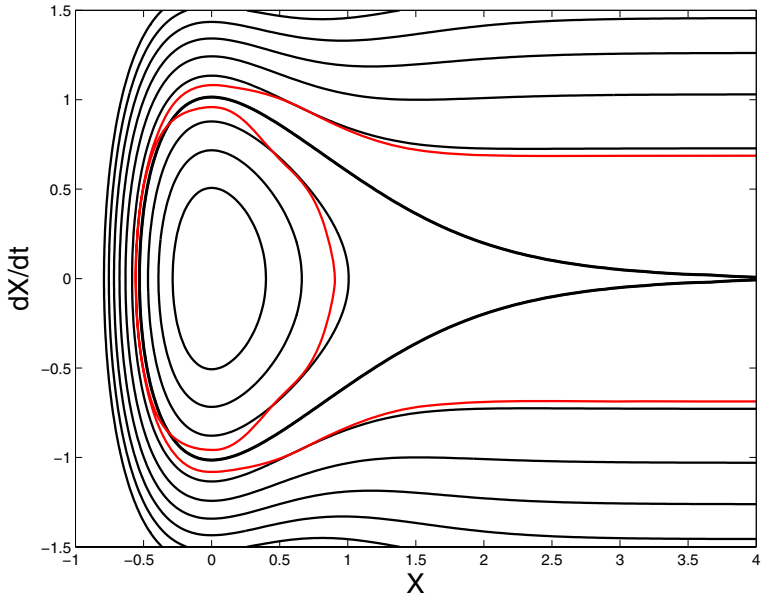

Figure 9. *The homoclinic orbit (bold) acts as a separatrix between unbounded orbits and closed bounded orbits for the unperturbed evolution equation. The orbits coincide with level sets of the energy of* (18)*, and the separatrix corresponds to* $E = 0$*. In red is overlaid the* X*-*$\dot{X}$ *projection of a two-bounce resonant solution with* $\epsilon = 0.3$ *and* $v_{\text{in}} = 0.687$*.*

is derived from (13b) by variation of parameters, shows that A is uniformly small when ω is large. Considering the X equation decoupled from A, the solutions lie along the level sets of the energy

$$E = \frac{MD(X)}{2}\dot{X}^2 + M(U(X) - 2). \tag{18}$$

The plot of Figure 9 shows that the two-dimensional phase space supports three types of orbits: unbounded orbits with positive energy that approach $X = \pm\infty$ with finite velocity as $X \to \infty$, bounded periodic orbits with negative energy, and between them a separatrix in the form of an orbit homoclinic to a degenerate saddle fixed point at $(X, \dot{X}) = (+\infty, 0)$, lying on the level set $E = 0$. The unbounded orbits correspond to kink-antikink pairs that reflect off each other, while the bounded periodic orbits describe a kink-antikink pair bound together to form a period breather solution. Without coupling to the mode $A(t)$, solutions cannot move from one side of the separatrix to the other. We employ a Melnikov integral method to measure the change in energy caused by the coupling to A [34].

With weak coupling, the black curves of Figure 9 are no longer invariant, and can be crossed, as is shown by the red curve in that figure. We employ a Melnikov integral to measure the change in energy over an approximately homoclinic orbit. We will show that the change in energy is small due to small coupling and the change of energy is at first negative (as (13) is a coupled Hamiltonian system with energy sharing). Thus, there is a small critical energy which we convert to a small critical velocity v_c. Solutions with this critical velocity and no energy in the $A(t)$ mode as $t \to -\infty$ lie on the stable manifold to the

set $\{(X,\dot{X},A,\dot{A})|X=+\infty,\ \dot{X}=0,$ and $\dot{A}^2+\omega^2A^2=Mv_c^2\}$. If the initial velocity is larger than v_c, then the interacting kink and antikink escape after the first bounce with their energy after interaction reduced by the amount calculated by the Melnikov integral. If the initial velocity is less than the critical velocity, then kink-antikink capture and other dynamics are possible. We will analyze this here.

A Melnikov integral often arises in showing the persistence of intersection between two invariant manifolds of a differential equation as a parameter is varied. If the unperturbed system has a conserved energy, then the distance between the two manifolds can be measured by the difference in energy between two solutions. By integrating the rate of change of distance along the unperturbed manifold, one arrives at the Melnikov integral. A zero of this integral indicates that the two manifolds intersect [26, 34]. In the present case, we are not looking for zeros of the integral but merely differences in energy. The formulas we derive later for resonant solutions can be thought of as finding zeros of a more complex multipart Melnikov integral.

To compute the approximate change in energy over one nearly homoclinic orbit, ΔE, first note that when coupled to the mode $A(t)$, the energy E given by (18) is now variable. By differentiating (18), we find its rate of change is given by

$$\begin{aligned}\frac{dE}{dt} &= M\dot{X}\left(2(1+I(X))\ddot{X}+I'(X)\dot{X}+U'(X)\right)\\ &= M\dot{X}\frac{2}{M^{3/2}}F'(X)A\\ &= \frac{2}{\sqrt{M}}A\frac{d}{dt}F(X).\end{aligned}\tag{19}$$

The total change in energy is thus given by

$$\Delta E=\int_{-\infty}^{\infty}\frac{2}{\sqrt{M}}A\frac{d}{dt}F(X)dt=-\frac{2}{\sqrt{M}}\int_{-\infty}^{\infty}F(X)\frac{dA}{dt}dt,\tag{20}$$

after an elementary integration by parts. Away from the degenerate fixed point at $(X,\dot{X})=(+\infty,0)$, the inner approximation (16) is valid, so that to leading order A depends on X but X evolves independently of A. Given that $\lim_{t\to-\infty}A=0$, we may solve for A by variation of parameters and find

$$A=\frac{1}{\omega\sqrt{M}}\left(-\cos\omega t\int_{-\infty}^{t}F(X(s))\sin\omega s\,ds+\sin\omega t\int_{-\infty}^{t}F(X(s))\cos\omega s\,ds\right).\tag{21}$$

Differentiating this with respect to time, and incorporating the result into (20), we find

$$\Delta E=-\frac{2}{M}\int_{-\infty}^{\infty}F(X(t))\left[\sin\omega t\int_{-\infty}^{t}F(X(s))\sin\omega s\,ds+\cos\omega t\int_{-\infty}^{t}F(X(s))\cos\omega s\,ds\right]dt.$$

Substitution of $u=\int_{-\infty}^{t}F(X(s))\sin\omega s\,ds$ in the first integral, and a similar substitution in

the second, converts ΔE into an elementary integral, which simplifies to

$$\Delta E = -\frac{1}{M}\left[\left(\int_{-\infty}^{\infty} F(X(t))\cos\omega t dt\right)^2 + \left(\int_{-\infty}^{\infty} F(X(t))\sin\omega t dt\right)^2\right] = -\frac{1}{M}\left|\int_{-\infty}^{\infty} F(X(t))e^{i\omega t}dt\right|^2. \tag{22}$$

Any trajectory with kinetic energy initially below the calculated value of ΔE will cross the separatrix into the region of bounded orbits—and be captured. Therefore the critical velocity is that for which the kinetic energy is exactly ΔE. As $X \to +\infty$, the energy approaches $M\dot{X}^2$. Therefore the kink-antikink pair will capture each other if $v < v_c$, where $Mv_c^2 = \Delta E$, i.e.,

$$v_c = \frac{1}{M}\left|\int_{-\infty}^{\infty} F(X(t))e^{i\omega t}dt\right|. \tag{23}$$

The integral (23) and those leading up to it could be calculated exactly using the (unknown) exact orbit $X(t)$. For large values of ω (small ϵ), the critical energy is small. Therefore $X(t)$ remains close to the homoclinic orbit. Thus we obtain an approximate value of ΔE by using the homoclinic orbit $X_S(t)$ in (23). Because (13) is autonomous, we may assume that $X_S(t)$ assumes its minimum at $t = 0$. Then $X_S(t)$ is even, and the complex exponential in the integral defining v_c may be replaced by the cosine.

In addition to calculating $v_c(\epsilon)$ empirically by repeated numerical solution of the model ODE (13), as described in Appendix A, we calculate the critical velocity by evaluating this integral in two ways. The first is numerical: along the homoclinic orbit, $\dot{X} \to 0$ as $X \to +\infty$, so the energy (18) is $E = M(U(+\infty) - 2 = 0$. Letting $B(X) = \frac{2-U(X)}{1+I(X)}$, we find along the separatrix for $t > 0$

$$\dot{X} = \sqrt{B(X)},\ X(0) = X_{\min}, \tag{24a}$$

where $X_{\min} \approx -.5299$ is the finite solution to $U(X) = 2$, the leftmost point along the homoclinic orbit. (For $t < 0$, $\dot{X} < 0$, so the other branch of the square root would be used.) Simultaneously, we solve the auxiliary equation

$$\dot{Y} = \frac{2}{M}F(X)\cos\omega t;\ Y(0) = 0. \tag{24b}$$

Then $X(t)$ is the solution along the separatrix and $\lim_{t\to\infty}|Y| = v_c$, comparing with (23), and using the even symmetry of the separatrix solution.

Under the assumption $\omega \gg 1$, we may also compute v_c asymptotically using the residue theorem, closing the contour in the upper half-plane. The dominant contribution to the integral comes from the poles nearest the real axis in the upper half-t-plane, which occur at $X_\pm = \pm i\pi/2\sqrt{2}$, where $|F| \to \infty$. The two poles in the t-plane are found by integrating (24a) numerically:

$$t_\pm = \pm T_r + iT_i = \pm\int_{X_{\min}}^{\pm\frac{i\pi}{2\sqrt{2}}} \frac{d}{X}\sqrt{B(X)} \approx \pm 0.6555 + 0.8787\,i. \tag{25}$$

Thus there are two poles that contribute terms of the same order asymptotically in the integral.

For simplicity, we will derive the series solution near t_+. The series about the other pole is obtained analogously and is related to it in a simple way although care must be taken in choosing the proper branches for the complex square root term. To obtain the series expansion for $F(X(t_+))$, we first find a series for $X - X_+$ in terms of $t - t_+$ by expanding $\sqrt{B(X)}$ in a Taylor series at X_+, where it is analytic. We insert this expansion into (24a) with the initial condition $X|_{t=t_+} = X_+$ and integrate. This series is inverted to give a series for $t - t_+$ in terms of $X - X_+$. Finally, this series is substituted into the Laurent series for $F(X)$ at $X = i\pi/2\sqrt{2}$,

$$F(X) = -\frac{3\pi}{8(X - \frac{i\pi}{2\sqrt{2}})^4} - \frac{\pi}{4(X - \frac{i\pi}{2\sqrt{2}})^2} + O(1),$$

to yield a Laurent series for $F(X(t))$ about $t = t_+$, which is then multiplied by $e^{i\omega t}$. The residue $\mathrm{Res}(F(X(t))e^{i\omega t}, t_+)$ is then given by the coefficient of $(t - t_+)^{-1}$ in the series form of this product.

The series about t_- is calculated the same way, using the other branch of the square root in integrating (24a). The residue at this pole is minus the conjugate of the residue at t_+, i.e., $\mathrm{Res}(F(X(t))e^{i\omega t}, t_-) = -\overline{\mathrm{Res}(F(X(t))e^{i\omega t}, t_+)}$, so by the Cauchy residue theorem, the two poles give a combined contribution to the integral $(2\pi i)2i\,\mathrm{Im}\,\mathrm{Res}(F(X(t))e^{i\omega t}, t_+)$, which is real, as it must be since the integral is real by the symmetry of $X(t)$. Contributions to the integral from additional poles located further north in the complex plane have not been computed, but would give corrections to this calculation.

This procedure is completed using Mathematica, and the expansion of the critical velocity is

(26)

$$\begin{aligned} v_c = \frac{\pi^2 e^{-\omega T_i}}{M} \Bigg| \mathrm{Im} \Bigg[e^{i\omega T_r} \Bigg(& -\frac{4i}{9(2i+\pi)^2}\omega^3 + \frac{-64 + 3\pi(2i+\pi)}{2\sqrt{12 - 6i\pi}(2i+\pi)^2}\omega^2 \\ & + \frac{-49152 + \pi(3328i + \pi(4700 + 9\pi(4i+\pi)))}{384(2i+\pi)^3}\omega \\ & + \frac{(2195456i + \pi(-185344 + \pi(-285440i + 3\pi(6440 + \ 3\pi(556i + 9(6 - i\pi)\pi)))))}{2048\sqrt{12 - 6\pi i}(2i+\pi)^3} \Bigg) \Bigg] \Bigg| \end{aligned}$$

or approximately

$$\begin{aligned} v_c = Me^{-\omega T_i} \Big| \mathrm{Im} \big[e^{i\omega T_r} \big(& (-2.714 - 4.565i) \ + (5.831 + 0.186i)\omega \\ & -(1.251 - 2.674i)\omega^2 - (0.287 + 0.134i)\omega^3 \big) \big] \Big| . \end{aligned}$$

The critical velocity is plotted in Figure 10 as a function of ϵ. In this figure, we plot the critical velocity as computed by three methods: direct numerical simulation of ODE (13) with initial conditions (14), numerical computation of the integral (23) via simulation of ODE (24), and evaluation of the integral via expansion (26). The quantitative agreement is excellent up to about $\epsilon = 0.2$, and the qualitative agreement is excellent up to $\epsilon = 1$, with the theoretical computation reproducing the surprising numerical discovery that the critical velocity varies

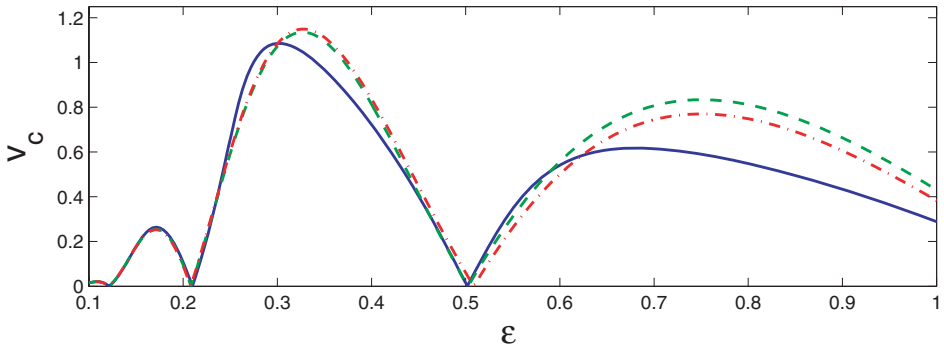

Figure 10. *The critical velocity, computed by direct numerical simulation (blue, solid), the numerical evaluation of integral (23) (green, dashed), and the contribution of the dominant poles of the integral, given in (26) (red, dash-dot).*

nonmonotonically and in fact vanishes altogether for at least three values of ϵ. We note in passing that all four terms computed in (26) were needed to obtain the good agreement seen in this figure.

The quantitative disagreement at $\epsilon = 1$, the physically relevant parameter value, is to be expected. By direct numerical simulation of (13), we find $v_c = 0.289$. Via numerical integration of the integral (23) using the ODE system (24), we find $v_{\text{integral}} = 0.4307$, and using the expansion (26), we find $v_{\text{residue}} = 0.3828$. The qualitative agreement, however, is so striking that we are confident that the mechanism of capture has been fully understood.

That the critical velocity depends on a parameter nonmonotonically is surprising, but not unprecedented, having been observed in another study of kink-antikink interactions in a nonlinear Klein–Gordon equation by Remoissenet and Peyrard [39]. That it vanishes for certain values of the parameter is even more surprising, but highlights the resonance mechanism of energy transfer. Equation (23) shows that the amount of energy transferred—Mv_c^2—is proportional to the square of the Fourier transform of $F(X(t))$ evaluated at the internal oscillation frequency ω. If the Fourier transform vanishes at a particular value of ω, no energy can be resonantly transferred to the internal oscillation, which is what happens in this case.

4.1. A generalization of the calculation for subsequent interactions. Each subsequent interaction involving an exchange of energy is described by a Melnikov integral consisting of the value previously calculated, plus an additional term depending on the amplitude and phase of $A(t)$ in a manner to be described below. If instead of vanishing as $t \to -\infty$,

$$A \sim \frac{\sqrt{M}v_c}{\omega}\mathcal{A}\sin\omega(t-\phi), \tag{27}$$

where the coefficient has been chosen for later convenience, then this adds an additional term to Melnikov integral (20) of the form $\Delta E_{\text{extra}} = -2Mv_c^2\mathcal{A}\cos\omega\phi$ and the total change in energy is given by

$$\Delta E = -Mv_c^2(1 + 2\mathcal{A}\cos\omega\phi). \tag{28}$$

Given that $A(t) \to 0$ as $t \to -\infty$, then for large values of t after the first interaction, (21) predicts that $A \sim \frac{\sqrt{M}v_c}{\omega} \sin \omega(t - t_1)$, where t_1 is taken to be the "symmetry time" of the first homoclinic orbit, the instant at which $\dot{X} = 0$. If the symmetry time on the second homoclinic orbit is given by t_2, then $\phi = t_2 - t_1$ and $\mathcal{A} = 1$. The second change of energy is given by

$$E_2 = E_1 - Mv_c^2(1 + 2\cos\omega(t_2 - t_1)), \tag{29}$$

and the combined change in energy is given by the sum of the two Melnikov integrals (22) and (28):

$$\Delta E_{\text{combined}} = -2Mv_c^2(1 + \cos\omega(t_2 - t_1)). \tag{30}$$

If the combined change in energy from (22) and (29) is zero, then after the second interaction all energy is returned to the propagating mode X and none resides in the oscillatory mode A. This will happen if $\cos\omega(t_2 - t_1) = -1$, i.e., if

$$t_2 - t_1 = \frac{(2n+1)\pi}{\omega}. \tag{31}$$

In the next section we show how to determine $t_2 - t_1$.

5. Matched asymptotic construction of two-bounce resonant solutions. If $v_{\text{in}} > v_c$, the trajectory does not cross from outside the separatrix to inside, so the kink and antikink do not capture each other but move apart after just one bounce. If $v_{\text{in}} < v_c$, the solution jumps to the inside of the separatrix and the kink and antikink will initially move apart and then will return to interact again. Following [21, 22], we will construct two-bounce solutions via a matched asymptotic expansion. Note that the energy is given by $E = 0$ along the separatrix orbit and is greater (smaller) on the exterior (interior) of the separatrix. The solution consists of near approaches to the degenerate saddle at $(X, \dot{X}) = (+\infty, 0)$. These are connected by homoclinic orbits. The near saddle-approaches are (slow time, in a manner to be made precise) outer solutions in a matched asymptotic expansion, and the homoclinic orbits are (fast time) inner solutions. Each outer solution orbit lies along a level set of the energy and is connected in forward and backward time to the homoclinic orbits. The difference in energy between two subsequent outer solutions is given by a Melnikov integral along the homoclinic inner solution connecting them. The Melnikov integral is dependent on the amplitude and phase of the mode $A(t)$ and thus differs on each subsequent bounce.

The matched asymptotic expansion of the two-bounce resonant solution consists of five components, as can be seen in Figure 11:

1. a near saddle-approach to $X = +\infty$ with energy $E_0 = Mv_{\text{in}}^2$, such that $\dot{X} \to v_{\text{in}} >$, $-v_c < v_{\text{in}} < 0$, as $t \searrow -\infty$;
2. a homoclinic orbit from one saddle-approach to the next satisfying $\dot{X}(t_1) = 0$, with energy change ΔE_1 given by (22);
3. a near saddle-approach to $X = +\infty$ with energy $E = -MW^2$, such that X achieves its maximum at $t = t^*$;
4. a homoclinic orbit from one saddle-approach to the next satisfying $\dot{X}(t_2) = 0$, with energy change ΔE_2 given by (28) with the phase ϕ to be explained below;

5. and a near saddle-approach to $X = \infty$ with positive energy $E = \frac{1}{2}v_{\text{out}}^2$, such that $\dot{X} \to v_{\text{out}}$, as $t \nearrow \infty$.

If $v_{\text{out}} = -v_{\text{in}}$, the solution will be called a two-bounce resonance. Nearby solutions which also escape to the positive energy region on the second bounce with energy E_2, satisfying $0 < E_2 < E_0$, will be called near resonances and give the resonance window its width. The change in energy calculated at step 4 might be insufficient to return enough energy to the propagating mode for it to cross the separatrix a second time. In that case, the trajectory stays inside the separatrix, repeating steps 3 and 4 until $E > Mv_c^2$ and the trajectory escapes to $X = +\infty$. The solution is an n-bounce resonance if $v_{\text{out}} = -v_{\text{in}}$ and the solution contains n inner expansions.

The change of energy at step 4 above is determined from the initial conditions using (28) with $\phi = t_2 - t_1$, obtained from the matching conditions between the solution at step 3 above with steps 2 and 4. The condition for an exact two-bounce resonance is given by (31). Because the cosine function is oscillatory, $t_2 - t_1$ in (31) must be known to $O(1)$, even though we will see that $t_2 - t_1$ is exponentially large for small values of ϵ.

Expansions of the two outer solutions that lie outside the separatrix will not be needed in determining $t_2 - t_1$, so we concentrate on expansions of the homoclinic orbit and of those with energy $E < Mv_c^2$.

5.1. The homoclinic orbit and its large X expansion. The differential equation for the homoclinic orbit is given above in (24a). We alter the initial condition slightly to $X(t_1) = X_{\min}$ for consistency with the framework above. We are interested in the large X expansion of this solution, which corresponds to the near saddle-approach to the degenerate saddle, so we expand $U(X)$ and $I(X)$ for $X \gg 1$ and find (to $O(1)$, the order that will be needed for matching)

$$\begin{aligned} U(X) &\sim 2 - 12e^{-2\alpha} + O(\alpha e^{-4\alpha}), \\ I(X) &\sim 12e^{-2\alpha}(\alpha - 1) + O(\alpha e^{-4\alpha}), \end{aligned} \tag{32}$$

where, recall, $\alpha = \sqrt{2}X$. Separating variables in (24a) yields an exact expression for the homoclinic orbit,

$$|t - t_1| = \int_{X_{\min}}^{X} \sqrt{\frac{1 + I(\bar{X})}{2 - U(\bar{X})}}\, d\bar{X}. \tag{33}$$

Using the expansion

$$\sqrt{\frac{1 + I(X)}{2 - U(X)}} \sim \frac{1}{\sqrt{12}} e^{\alpha} + +O(\alpha e^{-\alpha}), \tag{34}$$

the homoclinic also exactly satisfies

$$|t - t_1| = \int_{X_{\min}}^{X} \frac{1}{\sqrt{12}} e^{\sqrt{2}\bar{X}}\, d\bar{X} + \int_{X_{\min}}^{X} \left(\sqrt{\frac{1 + I(\bar{X})}{2 - U(\bar{X})}} - \frac{1}{\sqrt{12}} e^{\sqrt{2}\bar{X}} \right) d\bar{X}. \tag{35}$$

The first integral is evaluated explicitly:

$$\int_{X_{\min}}^{X} \frac{1}{\sqrt{12}} e^{\sqrt{2}\bar{X}}\, d\bar{X} = \frac{1}{\sqrt{24}} \left(e^{\sqrt{2}X} - e^{\sqrt{2}X_{\min}} \right). \tag{36}$$

The second integral is approximated for large X (as $X \to \infty$) by

$$\begin{aligned} &\int_{X_{\min}}^{X} \left(\sqrt{\frac{1+I(\bar{X})}{2-U(\bar{X})}} - \frac{1}{\sqrt{12}} e^{\sqrt{2}\bar{X}} \right) d\bar{X} \\ &\qquad \sim \int_{X_{\min}}^{\infty} \left(\sqrt{\frac{1+I(\bar{X})}{2-U(\bar{X})}} - \frac{1}{\sqrt{12}} e^{\sqrt{2}\bar{X}} \right) d\bar{X} + O\left(X e^{-\sqrt{2}X} \right). \end{aligned} \tag{37}$$

Let the constant integral on the right-hand side be denoted $\mathcal{I}$ and define $\mathcal{R} = \mathcal{I} - \frac{1}{\sqrt{24}} e^{\sqrt{2}X_{\min}}$, which is calculated numerically to be about $\mathcal{R} \approx 1.904$. Then the first homoclinic orbit, in a neighborhood of $X = +\infty$, may be expanded as

$$t - t_1 \sim \frac{1}{\sqrt{24}} e^{\sqrt{2}X} + \mathcal{R} + O\left(X e^{-\sqrt{2}X} \right) \text{ as } t - t_1 \to +\infty. \tag{38a}$$

Similarly, the second homoclinic orbit, characterized by its symmetry time t_2, satisfies

$$t_2 - t \sim \frac{1}{\sqrt{24}} e^{\sqrt{2}X} + \mathcal{R} + O\left(X e^{-\sqrt{2}X} \right) \text{ as } t - t_2 \to -\infty. \tag{38b}$$

5.2. The near saddle-approach and its finite time singularities. For large values of X, the outer scaling (17) applies, and the differential equation for X can be approximated by the unperturbed portion of the evolution, obtained by omitting the A-dependent term from (13a). Its energy is asymptotically constant, given by (18) with $E = -MW^2$, which we may write as

$$\dot{X} = \sqrt{\frac{2 - W^2 - U(X)}{1 + I(X)}} \sim \sqrt{12 e^{-2\sqrt{2}X} - W^2} \tag{39}$$

along with the initial condition that $U(X)|_{t=t^*} = 2 - W^2$. The leading-order part on the right side of (39) may be solved exactly by separation of variables to yield

$$\cos\left(\sqrt{2} W (t - t^*) \right) = \frac{W}{\sqrt{12}} e^{\sqrt{2}X}. \tag{40}$$

This equation expresses the scaling of the solutions at large X, which are a little bit unusual. They show that it is best not to scale X, but to scale $e^{\sqrt{2}X} = O\left(\frac{1}{W}\right)$, which implies that X is large, since W is small. Furthermore, we see that in this region $t - t^* = O\left(\frac{1}{W}\right)$. This is important because it implies, since t is large, that X evolves on a slow timescale in this region (relative to the fast timescale of the homoclinic orbit). These scales could have been determined directly from (39) above, but the exact solution (40) helps to make this

even clearer. Despite the fact that the leading-order component of X evolves slowly, the simultaneous fast oscillation of $A(t)$ will play an important role in what follows.

From the expansion (32), the potential exponentially decays as $X \to \infty$. The local phase portrait near this degenerate saddle point would show that these local solutions with negative local energy approach $X \to -\infty$ forward and backward in time. From the explicit general solution (40), these asymptotic behaviors as $X \to -\infty$ are seen to be finite time singularities, forward and backward in time, and we compute these times at which these singularities occur. For example, going backward in time from the near saddle-approach after the first pass, as $\sqrt{2}W(t-t^*) \to \pm\frac{\pi}{2}$, the left side of this equation vanishes, implying that $X \to -\infty$, leading to the singularity

$$t - t^* + \frac{\pi}{2\sqrt{2}W} \sim \frac{1}{\sqrt{24}} e^{\sqrt{2}X} \text{ as } t \searrow t^* - \frac{\pi}{2\sqrt{2}W}. \tag{41a}$$

Similarly, after the near saddle-approach,

$$-t + t^* + \frac{\pi}{2\sqrt{2}W} \sim \frac{1}{\sqrt{24}} e^{\sqrt{2}X} \text{ as } t \nearrow t^* + \frac{\pi}{2\sqrt{2}W}. \tag{41b}$$

Equation (41a) describes the finite time singularity that occurs in backward time. Note that as the left-hand side goes to zero, this forces $X \to -\infty$, and a similar statement holds for the forward-time singularity (41b).

5.3. Matching the homoclinic and near saddle-expansions. Let us describe in some detail first how (38a) connects to (41a). We wish to carefully explain the seemingly contradictory statement that in (38a), $X \to +\infty$, and in (41a), $X \to -\infty$. If interpreted incorrectly, this impression is always a danger in matching. In linear saddle point problems the exponential growth of the saddle-approach matches the exponential decay of the homoclinic orbit. Here the algebraic growth of the degenerate homoclinic orbit matches the finite time singularities. The asymptotic expansion (38a) is valid as $t \to \infty$ and asymptotic expansion (41a) is valid at t approaches the singularity backward in time. There should exist an elementary overlap region in which both are valid: X should be large with respect to its minimum on the homoclinic orbit, but far away from the maximum value obtained on the near saddle-approach. The functional forms are equal if $t^* - t_1 = \mathcal{R} + \frac{\pi}{2\sqrt{2}W}$ and similarly matching (38b) and (41b) $t_2 - t^* = \mathcal{R} + \frac{\pi}{2\sqrt{2}W}$. Combining these yields

$$t_2 - t_1 = 2\mathcal{R} + \frac{\pi}{\sqrt{2}W}. \tag{42}$$

This expresses the asymptotic expansion of the period, which increases without bound as the energy approaches zero from below. More importantly, (42) tells us how the time between the two bounces (asymptotically the center times of the two homoclinic orbits that describe the inner solutions) relates to the energy level upon which the saddle is approached. A diagram of the matching procedure for a two-bounce resonant solution is shown in Figure 11.

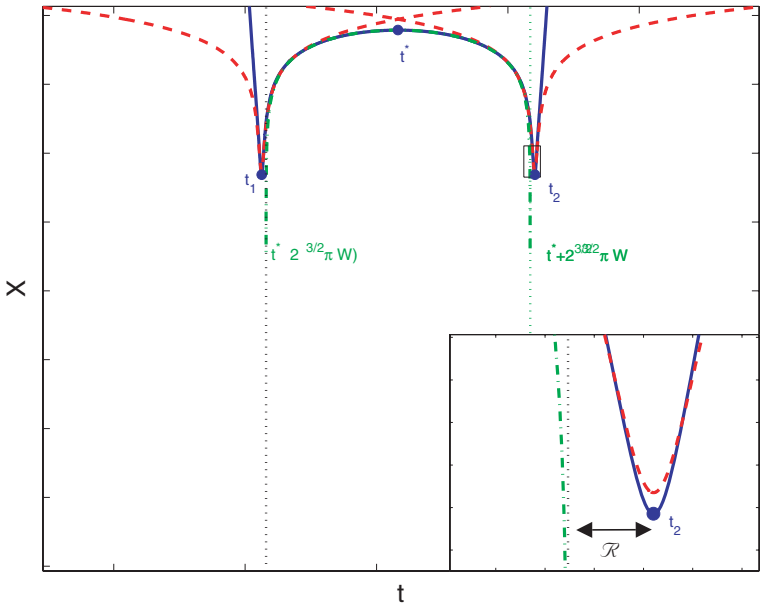

Figure 11. *The solution $X(t)$ (blue, solid), along with the inner, homoclinic, solutions (red, dashed), and the outer approximation, the negative-energy near saddle-approach (green, dash-dot). The homoclinic orbits are centered at t_1 and t_2, given by (38), and the near saddle-approach is centered at t^*, given by (40), and has vertical asymptotes at $t = t^* \pm \pi/2\sqrt{2}W$. The inset shows a close-up of the boxed region around t_2 and shows how the $O(1)$ constant $\mathcal{R}$ is used in the matching.*

5.4. Two-bounce resonant velocities. In order to obtain the exact two-bounce resonance, (42) must agree with (31) so that

$$W = \frac{1}{\sqrt{2}\left(\frac{2n+1}{\omega} - \frac{2\mathcal{R}}{\pi}\right)}.$$

Before the interaction, the energy in the propagating mode is $E = Mv_n^2$. After the interaction, the energy in the propagating mode is $E = -MW^2$, and according to the reasoning leading up to (23), they differ in energy by $\Delta E = Mv_c^2$. Therefore $v_n^2 - v_c^2 = -W^2$ so that

$$v_n = \sqrt{v_c^2 - \frac{1}{2}\left(\frac{2n+1}{\omega} - \frac{2\mathcal{R}}{\pi}\right)^{-2}}. \tag{43}$$

The theoretical and empirical values of v_n are plotted in Figure 12 for the case $\epsilon = 0.175$. In this figure, the empirical value of v_c is used rather than the asymptotic expansion (26). The agreement is of course best for small values of ϵ and v_c. The resonant velocity v_n is plotted against n for the case $\epsilon = 0.175$ which is chosen because the separation between the timescales in the two modes is large, yet the critical velocity is near a local maximum.

Formula (43) contains a wealth of information. As the critical velocity depends on ϵ, this explains how $n_{\min}$ depends on ϵ. The value of n in this equation must be large enough that the quantity under the square root is positive. This may be interpreted in reference to Figure 9.

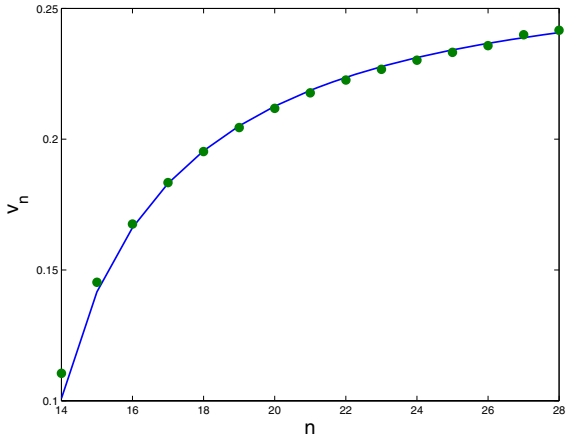

Figure 12. *The theoretical (line) and numerical values of the first* 15 *two-bounce resonant velocities of* (13) *with* $\epsilon = 0.175$.

The period of the closed bounded orbits on the interior of the homoclinic orbits diverges as their energy approaches the energy along the homocline, and this determines $t_2 - t_1$. When v_c is small, the trapped orbits must stay near the heteroclinic orbit (within a distance Mv_c^2 when measured using the energy). Therefore $t_2 - t_1$, and with it n, must be sufficiently large. As $n \to \infty$, the two-bounce resonant velocities accumulate at the critical value, $v_n \to v_c$, as seen from (43).

6. The separatrix map and its consequences. Of course, the above formula (43) applies only for a countable sequence of initial velocities (for almost no initial velocities, to put it in stark probabilistic terms)! Fortunately the analysis can easily be extended if we relax the condition that the changes in energy due to the first two interactions sum to zero. We follow ideas we first developed for propagation of a sine-Gordon kink past a defect [21] and interacting vector solitons for a coupled pair of nonlinear Schrödinger equations [22].

To generalize the results of section 5, we will need to know the energy $E(t)$ after a finite number of jumps, as well as information about the phase of $A(t)$. We first discuss $A(t)$. Along the first homoclinic (inner) solution, as $t - t_1 \to +\infty$, asymptotic evaluation of the variation of parameters formula (21) yields

$$A(t) \sim \frac{\sigma\sqrt{M}v_c}{\omega}\sin\omega(t-t_1) + \text{algebraically small nonoscillatory terms},$$

where v_c is given by (23), which is small beyond all orders in ω^{-1} by (26). The term $\sigma = \pm 1$ is given by $\sigma = \text{sign}\,(\int_{-\infty}^{\infty} F(X_S(t))\cos\omega t dt)$. As $t - t_j \to \infty$ along the jth homoclinic inner solution, this generalizes to:

$$A(t) \sim \frac{\sigma\sqrt{M}v_c}{\omega}\sum_{i=1}^{j}\sin\omega(t-t_i) + \text{algebraically small nonoscillatory terms}. \tag{44}$$

The algebraically small terms above do not play an important role in the dynamics, and we concentrate on the oscillatory terms. The appropriate generalization of energy change

formula (29) is given by

$$E_j = E_{j-1} - Mv_c^2 \left(1 + 2\sum_{i=1}^{j-1} \cos\omega(t_j - t_i)\right), \tag{45a}$$

where (t_j) is the sequence of bounce times and, as in (42),

$$t_j - t_{j-1} = 2\mathcal{R} + \frac{\pi}{\sqrt{4 - 2E_{j-1}/M}}. \tag{45b}$$

This is an example of a *separatrix map*, as has been widely studied, for example, in the book of Lichtenberg and Lieberman [31]. Taking the initial energy to be $E_0 = Mv_0^2$, (45a) may be summed over j. Using the identity $\cos 0 = 1$ and rearranging terms, we find the double sum:

$$E_n = Mv_0^2 - Mv_c^2 \sum_{i=1}^{n}\sum_{j=1}^{n} \cos\omega(t_j - t_i). \tag{46}$$

Therefore, an initial velocity lies in an n-bounce window if after $n-1$ bounces $E < 0$ but after n bounces $E > 0$. In between bounce j and bounce $j+1$, the energy is $E = -MW_j^2$. Equation (46) allows us to describe many further details of the fractal structure of the bounces, several of which we describe below.

Separatrix maps similar to (45) have been widely studied, and while the dynamics of the map will quickly diverge from the dynamics of the ODE system it approximates, they have been a valuable tool in the study of chaotic dynamics in Hamiltonian systems in the region of a so-called stochastic layer [31]. Such a map has also been termed the whisker map by Chirikov [12]. Rom-Kedar has constructed horseshoes for such separatrix maps, and the associated symbolic dynamics, in time-dependent Hamiltonian systems [40, 41]. Often such maps are studied by using Markov chains or other probabilistic methods to examine the statistical distributions of exit times [16, 33, 40]. In the present case this corresponds to the number of bounces preceding escape.

The separatrix map (45) appears at first to depend on the entire history of the trajectory, due to the summation term in (45a), but this sum could of course be simplified to $\mathcal{A}_0 \cos\omega(t - \mathcal{T}_0)$ by standard trigonometric identities. The map can further be reduced to two dimensions by restricting the dynamics to a level set of the Hamiltonian, and thus should be amenable to the types of analysis discussed briefly in the preceding paragraph. This analysis usually proceeds by identifying turnstile lobes in a perturbed separatrix, by which trajectories may pass from one region of the phase space to another. Because we are interested in the case where $A(t)$ is initially unexcited, we have instead found an expression for v_c which describes a complementary problem, and it is not useful for us to look on level sets of the Hamiltonian in order to explain phenomena such as Figure 6. By considering the case where $A(t)$ is excited before the first collision, and considering the restriction to a level set of the Hamiltonian, we could study the familiar lobe structure for the map (45) using E_j and $\mathcal{T}_j$ as the coordinates.

6.1. Width of the two-bounce windows. The two-bounce windows consist of all initial velocities less than v_c such that $E_2 > 0$. Therefore their edges are defined by the condition

that $E_2 = 0$. We look for the edge of the two-bounce window with velocity v_n, for which the time between the first and second bounce must be

$$\omega(t_2 - t_1) = (2n + 1 + \delta_n)\pi,$$

i.e., close to the time between bounces for the two-bounce resonance. Equation (46) then reduces to $0 = Mv_0^2 - Mv_c^2(2 - 2\cos\delta_n\pi)$, or

$$\cos\delta_n\pi = 1 - \frac{v_0^2}{2v_c^2}. \tag{47}$$

This, together with the Melnikov integral relating E_1 with v_0, defines δ_n and v_0 implicitly, but for large values of n, $v_0 \approx v_c$, so that $\cos\delta_n\pi \approx \frac{1}{2}$, or $\delta_{n\pm} \approx \pm\frac{1}{3}$. Thus the edges of the window occur approximately, for large n, when $\cos\delta_n\pi \approx \frac{1}{2}$, that is, $\delta_{n\pm} \approx \pm\frac{1}{3}$. Via the matching conditions, the left and right edges occur at

$$v_{n\pm} = \sqrt{v_c^2 - \frac{1}{2}\left(\frac{2n + 1 + \delta_{n\pm}}{\omega} - \frac{2\mathcal{R}}{\pi}\right)^{-2}}. \tag{48}$$

6.2. Other resonant solutions. We call a general solution an n-bounce resonance if after n bounces, all the energy resides in the translating mode and none in the oscillatory mode, i.e., if $E_n = Mv_0^2$ or

$$\sum_{i,j=1}^{n} \cos\omega(t_j - t_i) = 0. \tag{49}$$

Such solutions are highly symmetric, and their symmetry helps us to simplify this relationship. In particular, before the last bounce, the solution must have the correct amount of energy to return exactly to E_0. This implies that the energy in X before the final bounce must exactly equal the energy after the first bounce. A similar relation holds for the penultimate bounce and the second, and so on. We examine the three- and four-bounce resonant solutions in detail.

For the three-bounce resonance, $W_1 = W_2$, so $t_3 - t_2 = t_2 - t_1$, and (49) may be factored as $(2\cos\omega(t_2 - t_1) + 1)^2 = 0$, i.e.,

$$\cos\omega(t_2 - t_1) = -\frac{1}{2}, \text{ or } \omega(t_2 - t_1) = \left(2n + 1 \pm \frac{1}{3}\right)\pi. \tag{50}$$

Using our previous arguments about energy, this requires that

$$v_{n,3\pm} = \sqrt{v_c^2 - \frac{1}{2}\left(\frac{2n + 1 \pm \frac{1}{3}}{\omega} - \frac{2\mathcal{R}}{\pi}\right)^{-2}}.$$

Thus for each complete two-bounce resonance, there exists a pair of complete three-bounce resonances, one on either side. In fact this formula exactly matches formula (48) for the edges

of the two-bounce window as $n \to \infty$. As n gets large, then the three-bounce resonance windows line up increasingly close to the edges of the windows.

For the complete four-bounce resonance, $W_1 = W_3$, so $t_4 - t_3 = t_2 - t_1$, and, using trigonometric angle sum formulas, (49) factors as

$$(1 + \cos\omega(t_2 - t_1))(1 + \cos\omega(t_3 - t_1)) = 0. \tag{51}$$

Setting the first factor equal to zero yields the two-bounce resonance condition, so the four-bounce resonance condition is that $\omega(t_3 - t_1) = (2n_4 + 1)\pi$ for some $n_4 \in \mathbb{Z}$. There is no bound here on n_4. If v is between the nth and $n+1$th two-bounce windows, then there exists a four-bounce resonance solution for all $n_4 > n$ such that the corresponding formula for v does not lie inside a two-bounce resonance window. Similar formulae to (50) and (51) can be derived for complete resonances with a larger number of bounces, although they do not factor as nicely as (51). However, we will show numerically that the complete resonances do not tell the whole story of the fractal structure of multibounce windows.

6.3. The complete fractal structure. In this section we demonstrate numerically that (45) describes the entire intricate structure of the collective coordinates model of the kink-antikink interaction problem. Equation (45) gives a formula for the energy after $n+1$ bounces in terms of the energy after n bounces. If after n bounces $E_n > 0$, then the kink and antikink begin to move apart with velocity $v = \sqrt{\frac{E_n}{M}}$. For a fixed value of ϵ, we followed the trajectories of a large number of points between 0 and $v_c(\epsilon)$ and recorded two quantities for each: the number of bounces before the kink escaped and the velocity with which it escaped—the analogue of Figure 6.

The upper panel of Figure 13 shows all the reflection windows with up to four bounces, computed from the algebraic recursion relation. The lower panel is the result of direct numerical simulations of the model ODE system (13), as in Figure 6, but all solutions with greater than four bounces have been hidden, and the remaining portions of the curve color-coded by the number of bounces. It is clear that the algebraic recursion relation replicates the structure, if not the exact location, of all the windows. In addition, we see a much richer structure of three-bounce resonance windows surrounding each two-bounce window—very few of which correspond to complete resonances. Similarly, we find four-bounce windows surrounding each three-bounce window, and a whole hierarchy of narrower and narrower windows as we look increasingly closely at the structure (as demonstrated in Figure 14) which is responsible for the chaotic dependence on initial conditions. The many complete four-bounce resonances obtained as solutions to (51) form sequences that accumulate at the edges of the two-bounce windows, forming an additional piece of the fractal structure. Many more interesting features appear in the fractal landscape which we do not discuss here.

A further informative plot can be made in two dimensions. In Figure 15, the number of bounces before the kinks escape is plotted as a function of v and ϵ, computed using the separatrix map (45). This is plotted in Figure 15 using the value of $v_c(\epsilon)$ obtained by direct numerical simulation to compute ΔE in (45). Each colored region is analogous to the set of "middle thirds" that is deleted at a given step in the construction of the classical Cantor set. What remains at the end of this process is a measure-zero set of initial conditions that are unbounded as $t \to -\infty$ but bounded as $t \to +\infty$. We describe the fractal structure here in

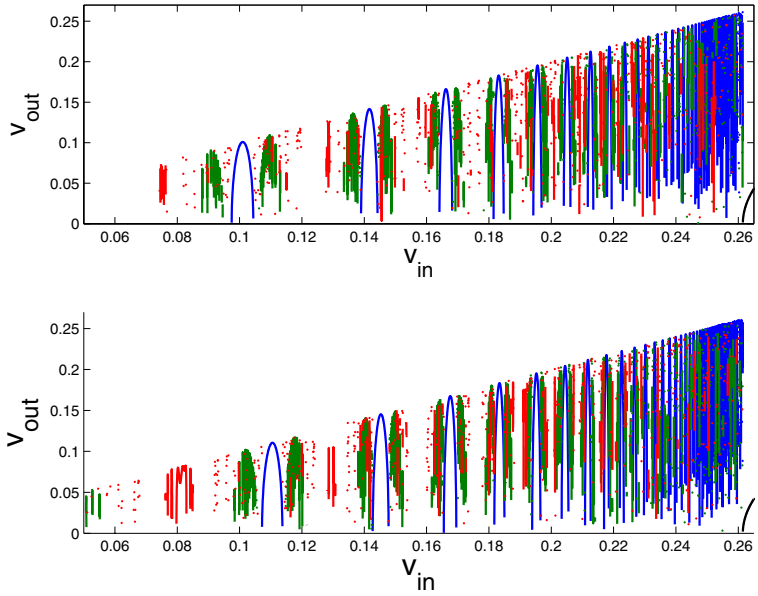

Figure 13. *The window structure due to recursion formula* (45) *(top) and due to direct numerical simulation (bottom).* 22501 *equally spaced values of* v *between* 0.05 *and* 0.275 *are used in each plot. Solutions that escape after* $1, 2, 3,$ *or* 4 *bounces are colored black, blue, green, and red, respectively.*

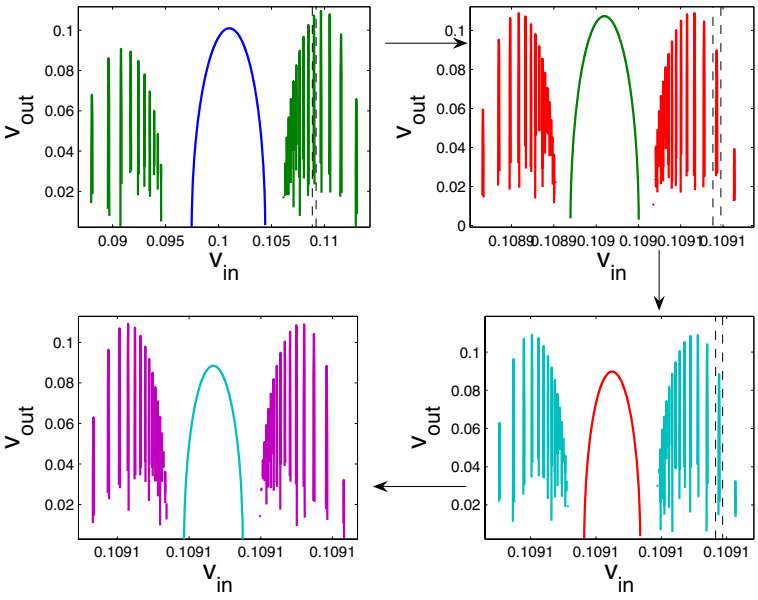

Figure 14. *Zooming in on the region surrounding the leftmost two-bounce window in the upper image of Figure* 13*. In the upper left image, only the two- and three-bounce windows are shown. Moving clockwise, in each successive figure we look at the region between the two dotted lines in the previous figure, seeing three- and four-bounce, four- and five-bounce, and five- and six-bounce resonance windows, respectively. The left and right edges of the final image are spaced only* $O(10^{-7})$ *apart.*

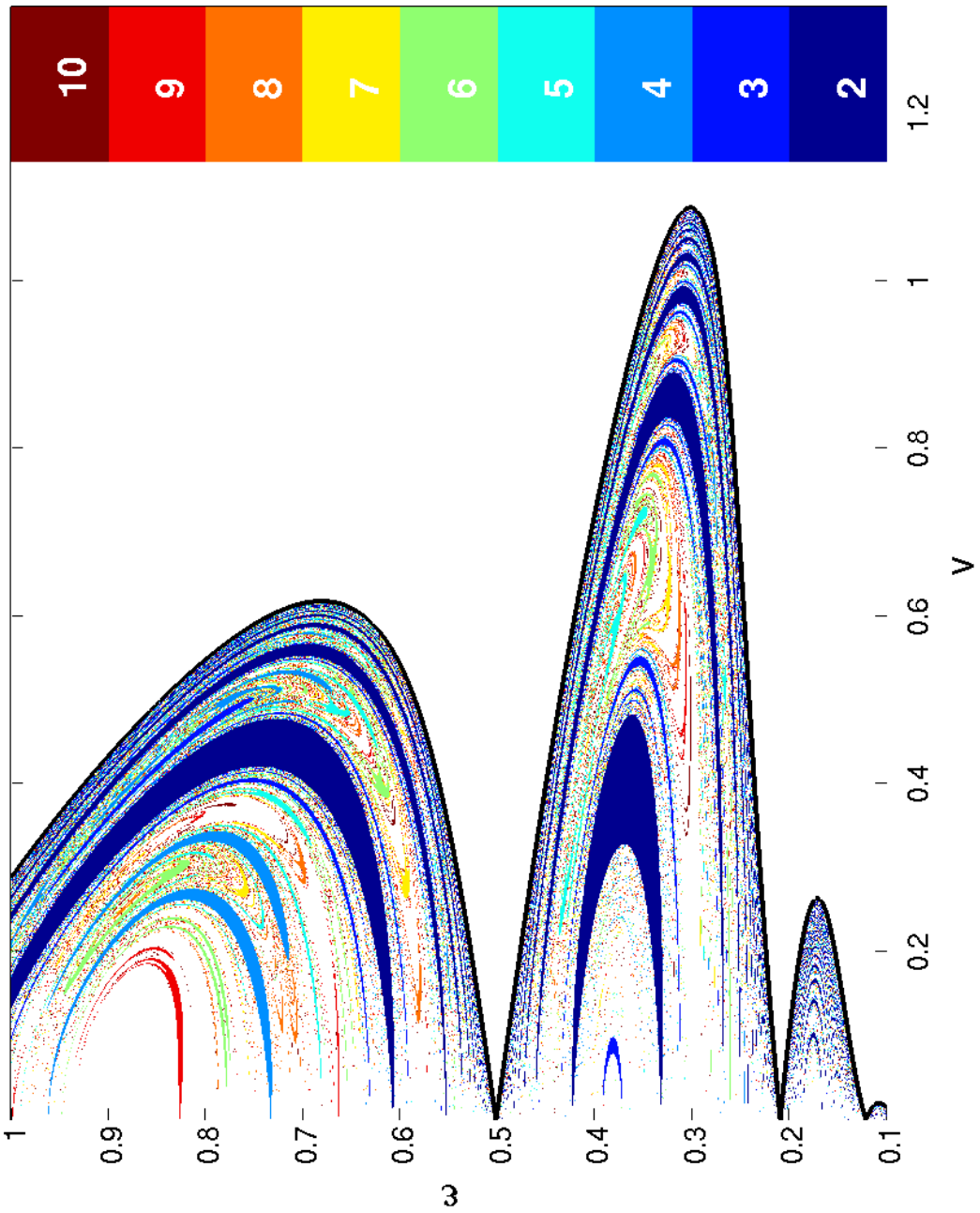

Figure 15. *The two-dimensional fractal structure arising from the recurrence relation (45). Dark blue patches represent the two-bounce windows, which appear and disappear as ϵ is varied. The black curve is the numerically calculated values of v_c (compare with Figure 10, axes reversed). All initial conditions with speeds greater than $v_c(\epsilon)$ (to the right) are reflected after just one bounce. The number of bounces in each window is indicated by the color bar on the right.*

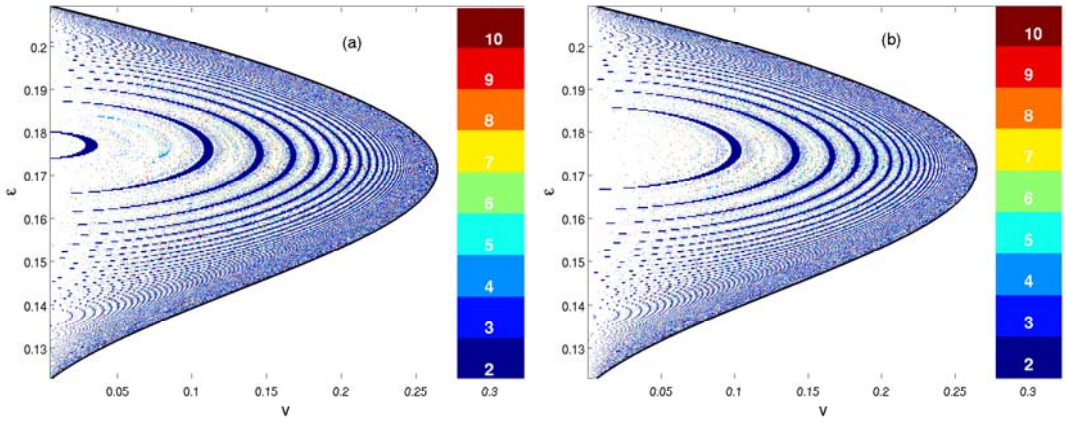

Figure 16. *The number of kink-antikink bounces before escape is plotted in false color against* ϵ *and* v_{in} *calculated using* (a) *over* 800,000 *direct numerical simulations of the ODE* (13) *and* (b) *the separatrix map* (45). *In both images, some spurious features occur near the outside edges of the figure due to aliasing (Moiré) effects.*

relatively simple terms and illustrations. Deeper analysis of the fractal and connection to the existing literature on fractals and homoclinic structures is the subject of ongoing research.

This fractal structure shows how windows appear and disappear as ϵ is varied, and may be used to predict parameter values where numerical experiments might unearth interesting behavior. For example, (45) predicts a wide four-bounce window for $\epsilon = 1$, centered about $v = 0.207$. Predictably, the quantitative agreement between experiment and theory is somewhat weak for large, physically relevant values of ϵ. For smaller values of ϵ the agreement is very good, as seen in Figure 16, although the fine structure is too delicate for one to observe anything but the two-bounce windows (streaks) at this resolution.

7. Conclusion. The two-bounce resonance in the ϕ^4 equation is a phenomenon with a long history that has traditionally been studied using informal reasoning based on resonance between a kink solution and an internal mode that oscillates around it. The purpose of this paper was to make precise the mechanism of this resonance in a finite-dimensional model of the kink-antikink interaction (13). We introduced an artificial small parameter ϵ into this model to allow us to use perturbation methods and found that this gives excellent quantitative agreement for smaller values of ϵ, and that the qualitative structure gives us insights into the behavior of even the physically relevant parameter value $\epsilon = 1$.

The major contribution of this paper is the demonstration that the two-bounce and multi-bounce resonance phenomena are related to phenomena in the separatrix map (45) derived here. Analyses of the consequences of this fact and the application of existing methods for such maps are ongoing topics of research, of which we have hardly scratched the surface.

Of course the derivation of the ODE system (13) is an uncontrolled approximation and should be considered as a finite-dimensional model of (1) rather than as an approximation to the full dynamics. In particular, the process leading to this equation neglects some important physics, namely, the loss of energy to radiation modes, clearly visible in Figure 1, and also makes the assumption that the kink solution maintains a constant width, in contrast with (2),

the exact formula for the kink. The soliton exhibits a length scale contraction proportional to $(1-v^2)^{-1/2}$, so a more complete theory for interactions causing the kink to accelerate should take this into account. Of course, the critical velocity in the PDE system is only $v_c \approx 0.26$, leading to a contraction of about 3.5%, so this should be a higher order correction. Nonetheless, studies of soliton interactions in nonlinear Schrödinger equations [45, 1] have found that width oscillations on their own are sufficient to produce the sorts of behavior seen here, even when those width oscillations do not correspond to any discrete eigenmode.

The phenomena described in this paper are in many ways generic and have been seen in many of the references already cited. We first developed the approach presented in the present paper in two previous papers [21, 22], although we have refined it significantly here. Most importantly we have recognized here that (45) approximately encodes the entire fractal structure and thus deserves further study as a dynamical system in its own right. We plan to look further at this and related systems.

The results of sections 4 through 6 are obtained via formal asymptotic expansions, and one might ask whether any of them can be made rigorous. A result of this type has been obtained by Camassa in a related system exhibiting multipulse homoclinic orbits [8]. He obtained a multipulse Melnikov integral for a two-degree-of-freedom system consisting of a pendulum coupled to a harmonic oscillator, with a form very similar to (13), and a change of energy formula for an initial pulse essentially identical to (22). He used this to demonstrate the existence of multibounce resonant solutions. Several technical issues, each surmountable by well-known methods, bar the direct application of Camassa's analysis. The first is that the homoclinic orbit of Figure 9 emanates from a degenerate fixed point at infinity, rather than a hyperbolic fixed point. A second issue is that the ϵ^{-1} scaling of frequency leads to exponentially small exchanges in energy between the two modes in (26). The Melnikov integral is formally derived as the leading-order term of a power series in ϵ, so the analysis necessary to show that this expansion is valid is a bit more involved than for the standard methods of [26].

Appendix A. Computational issues.

A.1. PDE simulations. We have used high-resolution numerics to solve the PDE (1) under initial condition (3). Because the even symmetry of the initial condition is preserved by the evolution, we solve the system on the interval $x \in [-L, 0]$, so that only the left half of each figure is actually computed. The Fourier transform of an even function contains only cosines, so it is natural after discretization to represent ϕ and ϕ_t by the coefficients of their discrete cosine transforms. If $\phi(x) = \sum_{k=0}^{N} \Phi_k \cos \frac{k\pi}{L}$, then $\phi_{xx} = \sum_{k=0}^{N} -k^2 \Phi_k \cos \frac{k\pi}{L}$, so this provides a convenient method for computing the spatial derivative. This method is accurate to beyond all orders in the grid spacing Δx, and as importantly, spectral methods are known to produce far less numerical dispersion and radiation than standard finite difference methods [46]. Forward and inverse cosine transforms are used at each step to compute the ϕ^3 terms, and every few steps when an output is required.

To compute the evolution in t, we use the fourth-order exponential time-differencing Runge–Kutta method (ETD-RK), introduced in [13] and rendered numerically stable by Kassam and Trefethen [28]. In this method the exponential of the linear operator is used to compute most of the stiff linear part of the evolution, while the nonlinear part of the equation

is computed by a Runge–Kutta method. This is done in a slightly different way than the more commonly used integrating factor method, generally with a much smaller error and less restriction on the time step. Writing the PDE (1) as a first-order system for ϕ and ϕ_t, the linear operator is given by

$$\mathcal{L} = \begin{pmatrix} 0 & 1 \\ \partial_x^2 + 1 & 0 \end{pmatrix},$$

which can be easily exponentiated using the cosine transform representation of the variables. If we partition the discretized operator into four blocks, then the nonzero elements of the operator are supported on the main diagonals of the off diagonal blocks. Its exponential contains terms along these diagonals and ones along the main diagonal. While the discretization of this PDE does not suffer from a severe Courant–Friedrichs–Levy restriction on the time step, this numerical method eliminates essentially all of the discretization errors, save those due to the nonlinear term.

Both numerical methods and processor speeds have made great strides in the twenty-plus years since the original investigation of this problem. Campbell, Schonfeld, and Wingate used second-order centered-differences in both space and time (i.e., the leapfrog method), and Anninos, Oliveira, and Matzner used fourth-order centered-differences in space and standard fourth-order Runge–Kutta in time. The first group found they needed to use $\Delta x = .01$ and $\Delta t = .009$, with the time step chosen to be slightly smaller to satisfy the CFL condition. In order to deal with the radiation produced by the low order discretization, they had to work on a very large computational domain. Anninos, Oliveira, and Matzner used $\Delta x = .08$ over the computational domain $[-40, 40]$, with $\Delta t \approx 0.7\Delta x$. By contrast, our computations were performed on the domain $[-32, 0]$ usually with 128 or 256 points in the discretization, so that $\Delta x = \frac{1}{4}$. A time step of $\Delta t = \frac{1}{8}$ or $\frac{1}{10}$ is adequate to reproduce Figure 2, though accurate computation of the windows in Figure 4 requires significantly finer discretization. The small amount of radiation visible in Figure 1 represents to high order the actual radiation present in the system and is not the result of the discretization. The width of the computational domain was chosen so that the radiation does not propagate through the periodic boundary and back to the front location in time to interfere with the two-bounce interaction, but this was actually found to be unimportant in the computation of the resonance windows.

A.2. ODE numerics. The ODE system (13) is fairly simple and can be integrated using off-the-shelf software. Both MATLAB and the Fortran package ODEPACK [27] were used at various times in this study, the latter especially when thousands of simulations were required. The only difficulty is the removable singularities of the potential functions near $X = 0$, where a high order Taylor polynomial was used to obtain smooth function values.

Of more interest is the method used to calculate critical velocities in Figure 10. As Figure 6 shows, the output speed just above the critical velocity scales as $v_{\text{out}} \approx C\sqrt{v_{\text{in}}^2 - v_{\text{c}}^2}$. A modified secant method is used to find v_{c}. Two input velocities $v_{2,\text{in}} > v_{1,\text{in}} > v_{\text{c}}$ are chosen, and a secant method iteration is performed using the two corresponding values of v_{out}^2. This produces a new input velocity v_{guess}. A new initial value problem is simulated with this value of v and is terminated when one of two things happens. If the kink escapes after one bounce, then the secant method is continued. We can tell if the kink is captured if it turns around toward its second bounce, i.e., if the $X(t)$ has two local minima. In this case, a bisection

method is used to find a new one-bounce solution between the current value of v and the smallest known value of v leading to escape. In this way we are able to generate a smooth curve of critical velocities for Figure 10 without exhaustively searching for v_c at each fixed value of ϵ.

We compute precise values of the resonant velocities v_n by numerically minimizing, with respect to v_{in}, the A-energy, $E_A = \omega^2 A^2 + \dot{A}^2$ when X reaches a predetermined large value. We locate the instant at which each bounce takes place for the computation of $t_2 - t_1$ using the event-location feature of the DLSODAR subroutine of ODEPACK, and find in this manner that (31) is very accurate.

Acknowledgments. We would like to thank Robert Miura for information about the history of solitons, and Panayotis Kevrekidis for pointing out the work of Peyrard and Remoissenet, as well as Gregor Kovacic and Vered Rom-Kedar for information about separatrix maps.

REFERENCES

[1] F. Kh. Abdullaev, A. Gammal, and L. Tomio, *Dynamics of bright matter-wave solitons in a Bose-Einstein condensate with inhomogeneous scattering length*, J. Phys. B, 37 (2004), pp. 635–651.
[2] M. J. Ablowitz and P. A. Clarkson, *Solitons, Nonlinear Evolution Equations and Inverse Scattering*, London Math. Soc. Lecture Note Ser. 149, Cambridge University Press, Cambridge, UK, 1991.
[3] M. J. Ablowitz, M. D. Kruskal, and J. F. Ladik, *Solitary wave collisions*, SIAM J. Appl. Math., 36 (1979), pp. 428–437.
[4] P. Anninos, S. Oliveira, and R. A. Matzner, *Fractal structure in the scalar $\lambda(\phi^2-1)^2$ model*, Phys. Rev. D, 44 (1991), pp. 1147–1160.
[5] T. Belova and A. Kudryavtsev, *Quasi-periodic orbits in the scalar classical $\lambda\phi^4$ field theory*, Phys. D, 32 (1988), pp. 18–26.
[6] N. Bilas and N. Pavloff, *Dark soliton past a finite size obstacle*, Phys. Rev. A, 72 (2005), 033618; also available online from http://link.aps.org/abstract/PRA/v72/e033618.
[7] D. Cai, A. R. Bishop, and N. Gronbech-Jensen, *Resonance in the collision of two discrete intrinsic localized excitations*, Phys. Rev. E, 56 (1997), pp. 7246–7252.
[8] R. Camassa, *On the geometry of an atmospheric slow manifold*, Phys. D, 84 (1995), pp. 357–397.
[9] D. K. Campbell and M. Peyrard, *Kink-antikink interactions in the double sine-Gordon equation*, Phys. D, 19 (1986), pp. 165–205.
[10] D. K. Campbell and M. Peyrard, *Solitary wave collisions revisited*, Phys. D, 18 (1986), pp. 47–53.
[11] D. K. Campbell, J. S. Schonfeld, and C. A. Wingate, *Resonance structure in kink-antikink interactions in ϕ^4 theory*, Phys. D, 9 (1983), pp. 1–32.
[12] B. V. Chirikov, *A universal instability of many-dimensional oscillator systems*, Phys. Rep., 52 (1979), pp. 264–379.
[13] S. M. Cox and P. C. Matthews, *Exponential time differencing for stiff systems*, J. Comput. Phys., 176 (2002), pp. 430–455.
[14] Y. Doi, *Energy exchange in collisions of intrinsic localized modes*, Phys. Rev. E, 68 (2003), 066608.
[15] P. G. Drazin and R. S. Johnson, *Solitons: An introduction*, Cambridge University Press, Cambridge, UK, 1993.
[16] R. W. Easton, J. D. Meiss, and S. Carver, *Exit times and transport for symplectic twist maps*, Chaos, 3 (1993), pp. 153–165.
[17] Z. Fei, Y. S. Kivshar, and L. Vázquez, *Resonant kink-impurity interactions in the ϕ^4 model*, Phys. Rev. A, 46 (1992), pp. 5214–5220.
[18] Z. Fei, Y. S. Kivshar, and L. Vázquez, *Resonant kink-impurity interactions in the sine-Gordon model*, Phys. Rev. A, 45 (1992), pp. 6019–6030.

[19] B. F. Feng, Y. Doi, and T. Kawahara, *Quasi-continuum approximation for discrete breathers in Fermi–Pasta–Ulam atomic chains*, J. Phys. Soc. Japan, 73 (2004), pp. 2100–2111.
[20] C. S. Gardner, J. M. Greene, M. D. Kruskal, and R. M. Miura, *Method for solving the Korteweg-de Vries equation*, Phys. Rev. Lett., 19 (1967), pp. 1095–1097.
[21] R. H. Goodman and R. Haberman, *Interaction of sine-Gordon kinks with defects: The two-bounce resonance*, Phys. D, 195 (2004), pp. 303–323.
[22] R. H. Goodman and R. Haberman, *Vector soliton interactions in birefringent optical fibers*, Phys. Rev. E, 71 (2005), 055065.
[23] R. H. Goodman, P.J. Holmes, and M.I. Weinstein, *Interaction of sine-Gordon kinks with defects: Phase space transport in a two-mode model*, Phys. D, 161 (2002), pp. 21–44.
[24] R. H. Goodman, R. E. Slusher, and M. I. Weinstein, *Stopping light on a defect*, J. Opt. Soc. Amer. B Opt. Phys., 19 (2002), pp. 1635–1632.
[25] C. Gorria, Yu. B. Gaididei, M. P. Soerensen, P. L. Christiansen, and J. G. Caputo, *Kink propagation and trapping in a two-dimensional curved Josephson junction*, Phys. Rev. B, 69 (2004), 134506.
[26] J. Guckenheimer and P. Holmes, *Nonlinear oscillations, dynamical systems, and bifurcations of vector fields*, Springer-Verlag, New York, 1983.
[27] A. C. Hindmarsh, *ODEPACK, a systematized collection of ODE solvers*, in Scientific Computing, R. S. Stepleman, ed., IMACS Trans. Sci. Comput. 1, IMACS, New Brunswick, NJ, 1983, pp. 55–64.
[28] A.-K. Kassam and L. N. Trefethen, *Fourth order time-stepping for stiff PDEs*, SIAM J. Sci. Comput., 26 (2005), pp. 1214–1233.
[29] P. G. Kevrekidis and S. V. Dmitriev, *Collisions*, in The Encyclopedia of Nonlinear Science, A. Scott, ed., Routledge, New York, 2004, pp. 148–150.
[30] Y. S. Kivshar, Z. Fei, and L. Vázquez, *Resonant soliton-impurity interactions*, Phys. Rev. Lett., 67 (1991), pp. 1177–1180.
[31] A. J. Lichtenberg and M. A. Lieberman, *Regular and Chaotic Dynamics*, Springer-Verlag, New York, 1992.
[32] B. A. Malomed, *Variational methods in nonlinear fiber optics and related fields*, Prog. Opt., 43 (2002), pp. 71–193.
[33] J. D. Meiss, *Average exit times for volume-preserving maps*, Chaos, 7 (1997), pp. 139–147.
[34] V. K. Melnikov, *On the stability of the center for time periodic perturbations*, Trans. Moscow Math. Soc., 12 (1963), pp. 1–57.
[35] A. C. Newell, *Solitons in Mathematics and Physics*, CBMS-NSF Regional Conf. Ser. in Appl. Math. 48, SIAM, Philadelphia, PA, 1985.
[36] I. E. Papacharalampous, P. G. Kevrekidis, B. A. Malomed, and D. J. Frantzeskakis, *Soliton collisions in the discrete nonlinear Schrödinger equation*, Phys. Rev. E, 68 (2003), 046604.
[37] J. K. Perring and T. H. R. Skyrme, *A model unified field equation*, Nuclear Phys., 31 (1962), pp. 550–555.
[38] M. Peyrard and D. K. Campbell, *Kink-antikink interactions in a modified sine-Gordon model*, Phys. D, 9 (1983), pp. 33–51.
[39] M. Remoissenet and M. Peyrard, *Soliton dynamics in new models with parameterized periodic double-well and asymmetric substrate potentials*, Phys. Rev. B, 29 (1984), pp. 3153–3166.
[40] V. Rom-Kedar, *Transport rates of a class of two-dimensional maps and flows*, Phys. D, 43 (1990), pp. 229–268.
[41] V. Rom-Kedar, *Homoclinic tangles—classification and applications*, Nonlinearity, 7 (1994), pp. 441–473.
[42] J. S. Russell, *Report on waves*, Rep. 14th Meet. Brit. Assoc. Adv. Sci., John Murray, 1844.
[43] A. Scott, *Solitons, a brief history*, in The Encyclopedia of Nonlinear Science, A. Scott, ed., Routledge, New York, 2004, pp. 852–855.
[44] T. Sugiyama, *Kink-antikink collisions in the two-dimensional ϕ^4 model*, Prog. Theor. Phys., 61 (1979), pp. 1550–1563.
[45] Y. Tan and J. Yang, *Complexity and regularity of vector-soliton collisions*, Phys. Rev. E, 64 (2001), 056616.
[46] L. N. Trefethen, *Spectral methods in MATLAB*, Software Environ. Tools 10, SIAM, Philadelphia, 2000.

[47] T. Ueda and W. L. Kath, *Dynamics of coupled solitons in nonlinear optical fibers*, Phys. Rev. A, 42 (1990), pp. 563–571.
[48] K. Yagasaki, *Horseshoes in two-degree-of-freedom Hamiltonian systems with saddle-centers*, Arch. Ration. Mech. Anal., 154 (2000), pp. 275–296.
[49] K. Yagasaki and T. Wagenknecht, *Detection of symmetric homoclinic orbits to saddle-centres in reversible systems*, preprint, 2005.
[50] J. Yang and Y. Tan, *Fractal structure in the collision of vector solitons*, Phys. Rev. Lett., 85 (2000), pp. 3624–3627.
[51] N. J. Zabusky and M. D. Kruskal, *Interactions of solitons in a collisionless plasma and the recurrence of initial states*, Phys. Rev. Lett., 15 (1965), pp. 240–243.